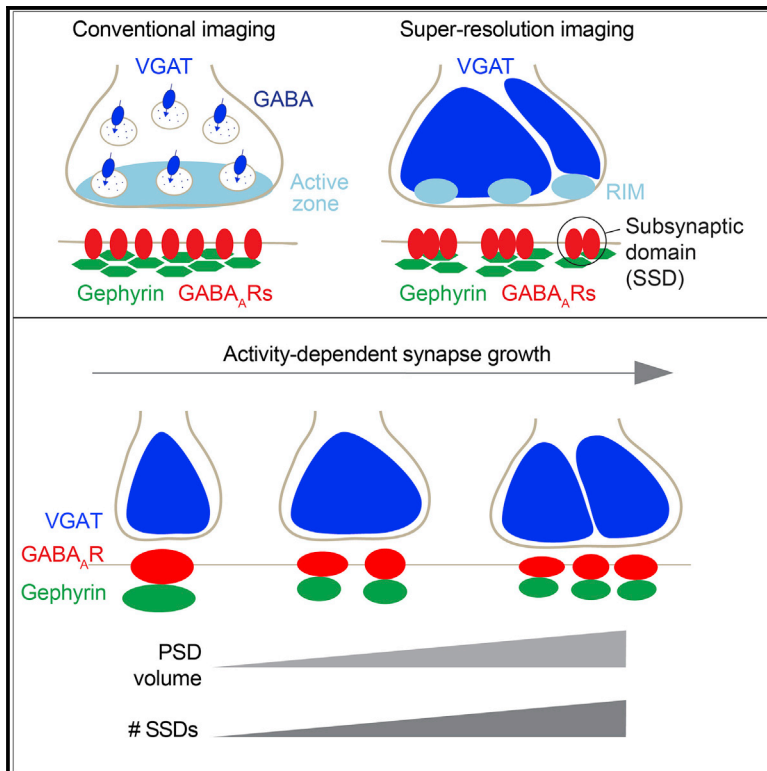**Article**

Nanoscale Subsynaptic Domains Underlie the Organization of the Inhibitory Synapse

Graphical Abstract

Authors

Kevin C. Crosby, Sara E. Gookin, Joshua D. Garcia, Katlin M. Hahm, Mark L. Dell'Acqua, Katharine R. Smith

Correspondence

katharine.r.smith@ucdenver.edu

In Brief

Crosby et al. reveal that inhibitory synapses are composed of nanoscale subsynaptic domains of $GABA_A$ receptors, the inhibitory scaffold gephyrin and the active-zone protein RIM. During plasticity, additional subsynaptic domains are recruited to the synapse, suggesting a mechanism for activity-dependent synaptic growth.

Highlights

- Inhibitory synapses are composed of nanoscale subsynaptic domains (SSDs)

- Gephyrin and $GABA_A$R SSDs closely associate and are dependent on each other

- $GABA_A$R SSDs are closely associated with presynaptic active-zone SSDs

- Inhibitory synapses recruit additional SSDs during activity-dependent growth

CellPress

Nanoscale Subsynaptic Domains Underlie the Organization of the Inhibitory Synapse

Kevin C. Crosby,[1] Sara E. Gookin,[1] Joshua D. Garcia,[1] Katlin M. Hahm,[1] Mark L. Dell'Acqua,[1] and Katharine R. Smith[1,2,*]
[1]Department of Pharmacology, University of Colorado School of Medicine, Aurora, CO 80045, USA
[2]Lead Contact
*Correspondence: katharine.r.smith@ucdenver.edu
https://doi.org/10.1016/j.celrep.2019.02.070

SUMMARY

Inhibitory synapses mediate the majority of synaptic inhibition in the brain, thereby controlling neuronal excitability, firing, and plasticity. Although essential for neuronal function, the central question of how these synapses are organized at the subsynaptic level remains unanswered. Here, we use three-dimensional (3D) super-resolution microscopy to image key components of the inhibitory postsynaptic domain and presynaptic terminal, revealing that inhibitory synapses are organized into nanoscale subsynaptic domains (SSDs) of the gephyrin scaffold, GABA$_A$Rs and the active-zone protein Rab3-interacting molecule (RIM). Gephyrin SSDs cluster GABA$_A$R SSDs, demonstrating nanoscale architectural interdependence between scaffold and receptor. GABA$_A$R SSDs strongly associate with active-zone RIM SSDs, indicating an important role for GABA$_A$R nanoscale organization near sites of GABA release. Finally, we find that in response to elevated activity, synapse growth is mediated by an increase in the number of postsynaptic SSDs, suggesting a modular mechanism for increasing inhibitory synaptic strength.

INTRODUCTION

Inhibitory synapses are the major sites of GABAergic inhibition in the brain and are critical for controlling neuronal excitability, firing, and synaptic plasticity (Flores and Méndez, 2014; Klausberger and Somogyi, 2008). Disruption of inhibitory synaptic function changes the excitatory-inhibitory balance of neurons and circuits, altering behavior and contributing to numerous brain pathologies (Blundell et al., 2009; Papadopoulos et al., 2007; Tretter et al., 2009; Yizhar et al., 2011). Inhibitory synapses exhibit extensive synaptic plasticity, which alters the strength and efficacy of synaptic inhibition (Flores and Méndez, 2014; Petrini and Barberis, 2014). A major postsynaptic determinant of inhibitory synapse strength is the number of GABA$_A$ receptors (GABA$_A$Rs) clustered at the synapse (Luscher et al., 2011; Nusser et al., 1998). Therefore, defining the mechanisms by which synaptic GABA$_A$Rs are stabilized at synaptic sites, and how their clustering is altered in synaptic plasticity, is crucial for understanding neuronal inhibition and its disruption in brain

disorders (Luscher et al., 2011; Smith and Kittler, 2010). Despite the importance of inhibitory synaptic plasticity for myriad neuronal and network functions, the mechanisms that underlie inhibitory structural synaptic plasticity are poorly understood.

Modern super-resolution microscopy techniques have revealed that postsynaptic density proteins and AMPA receptors (AMPARs) in excitatory synapses are organized into nanoscale subsynaptic domains (Fukata et al., 2013; Hruska et al., 2018; MacGillavry et al., 2013; Nair et al., 2013). This arrangement places AMPARs in the optimal position for efficient activation, opposite presynaptic glutamate release sites, and is proposed to be critical for efficient synaptic transmission (Biederer et al., 2017; Haas et al., 2018; MacGillavry et al., 2013; Sinnen et al., 2017; Tang et al., 2016). Moreover, nanoscale alterations to synapse substructure and composition are thought to significantly affect synaptic efficacy and synaptic plasticity (Biederer et al., 2017; Chen et al., 2018; MacGillavry and Hoogenraad, 2015; MacGillavry et al., 2013; Nair et al., 2013; Purkey et al., 2018; Sinnen et al., 2017; Smith et al., 2014b; Tang et al., 2016; Tønnesen et al., 2014). In contrast with excitatory synapses, our understanding of the nanoscale organization of inhibitory synapses remains rudimentary. Two recent studies using photo-activated localization microscopy (PALM) have shown that the inhibitory postsynaptic scaffolding protein gephyrin forms subsynaptic nanodomains (Pennacchietti et al., 2017; Specht et al., 2013). However, how gephyrin nanoscale organization relates to GABA$_A$R nanoscale positioning in the postsynaptic domain and in relation to the distribution of proteins of the inhibitory axon terminal remains unknown.

Here, we have used three-dimensional structured illumination microscopy (3D-SIM) combined with computational geometric analysis of object-segmented features to fully characterize the nanoscale organization of the inhibitory synapse. By imaging synaptic GABA$_A$Rs, gephyrin, and inhibitory presynaptic terminals (labeled with VGAT or Rab3-interacting molecule [RIM]), we reveal that the inhibitory synapse is composed of nanoscale subsynaptic domain (SSD) structures. We find that gephyrin SSDs cluster GABA$_A$R SSDs at the inhibitory postsynaptic site and are interdependent on each other. Importantly, GABA$_A$R SSDs strongly associate with RIM SSDs in the active zone, suggesting that GABA$_A$Rs are clustered in close proximity to sites of presynaptic release. Furthermore, SSDs likely represent building blocks for the inhibitory synapses as gephyrin and GABA$_A$R SSDs emerge coincident with synapse growth during homeostatic synaptic scaling-up. Together, these data implicate nanoscale SSD organization at the inhibitory synapse as a key mechanism
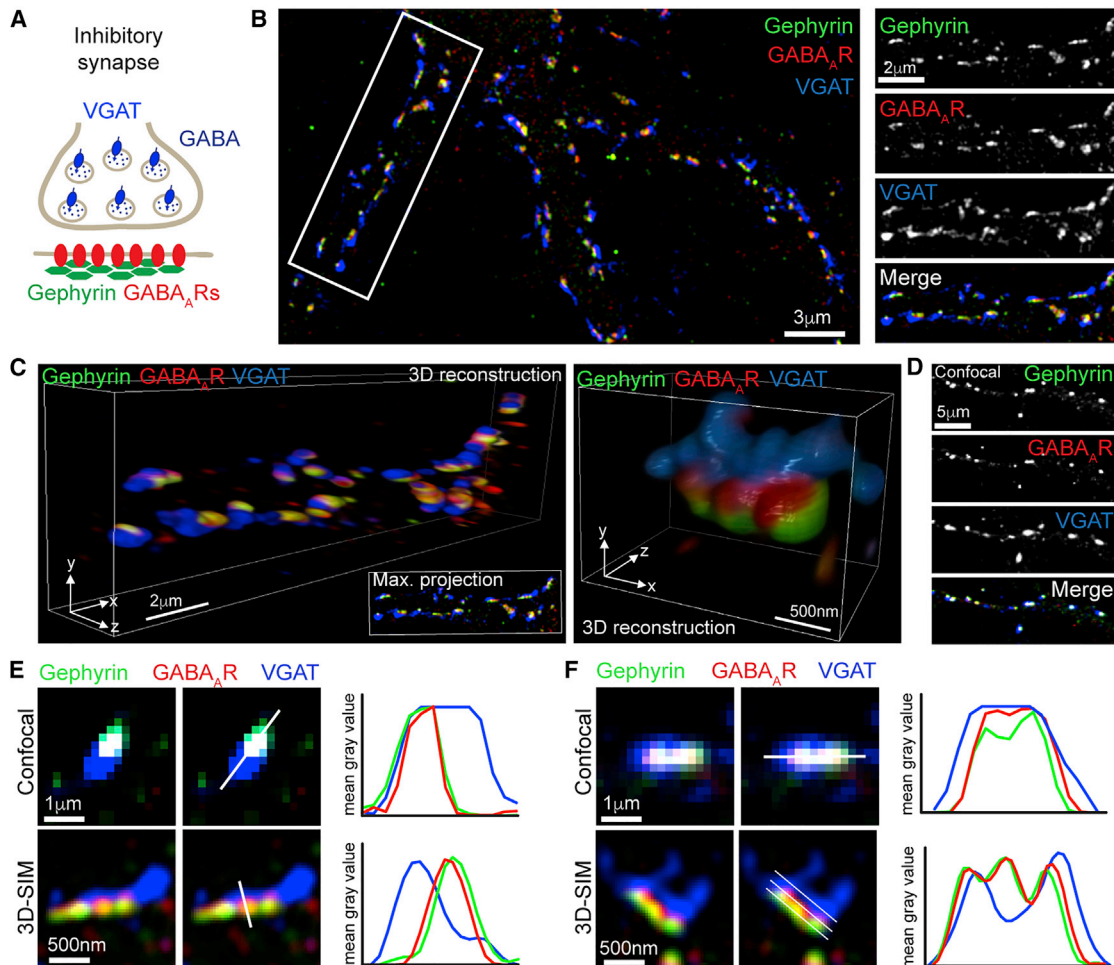
Figure 1. 3D-SIM of Inhibitory Synapses

(A) Schematic of the inhibitory synapse showing that synaptic GABA$_A$Rs are anchored by gephyrin opposite GABAergic terminals labeled with VGAT.

(B) Three-dimensional structured illumination microscopy (3D-SIM) maximum projection of hippocampal neuron labeled with antibodies to gephyrin (green), GABA$_A$Rs (red), and VGAT (blue); region in white box is the dendrite on the right.

(C) 3D reconstructions of the dendrite in (B) and a single synapse. Also see Video S1.

(D) Confocal maximum projection of hippocampal neuron stained under identical conditions to (B).

(E and F) Magnifications of synapses from confocal and SIM images, with line scans perpendicular (E) or parallel (F) to the synapse axis, showing nanoscale subsynaptic domains (SSDs) in the SIM image. White lines show path of line scans.

for GABA$_A$R stabilization at the postsynaptic site near presynaptic sites of neurotransmitter release and underscore SSDs as potential building blocks for altering synapse strength during plasticity.

RESULTS

3D, Three-Color Super-resolution Imaging of the Inhibitory Synapse

To determine the nanoscale organization of the inhibitory synapse, we used three-color 3D SIM, which provides an enhanced resolution of ~120 nm laterally and ~300 nm axially (Figure 1; Video S1). We imaged surface GABA$_A$Rs and gephyrin clusters on hippocampal neuronal dendrites, along with a presynaptic inhibitory marker, vesicular GABA transporter (VGAT), to label

inhibitory axon terminals (Figures 1A and 1B). Because of the 3D nature of SIM, we could reconstruct dendrites and individual synapses in three dimensions, enabling unprecedented volumetric visualization of inhibitory synapses at the nanoscale level (Figure 1C; Video S1). A comparison of 3D SIM images with similar confocal microscopy images showed that 3D SIM reveals substantially more detail than conventional confocal images (Figures 1D–1F). Line scans perpendicular to the synapse axis through 3D SIM and confocal synapse zooms show that 3D SIM is clearly able to delineate between the pre- and postsynaptic site, whereas confocal images do not (Figure 1E). Furthermore, parallel line scans through the synapse axis of 3D SIM-imaged inhibitory synapses indicate that the inhibitory synapse is not a homogeneous structure and that each compartment of the synapse is composed of one or
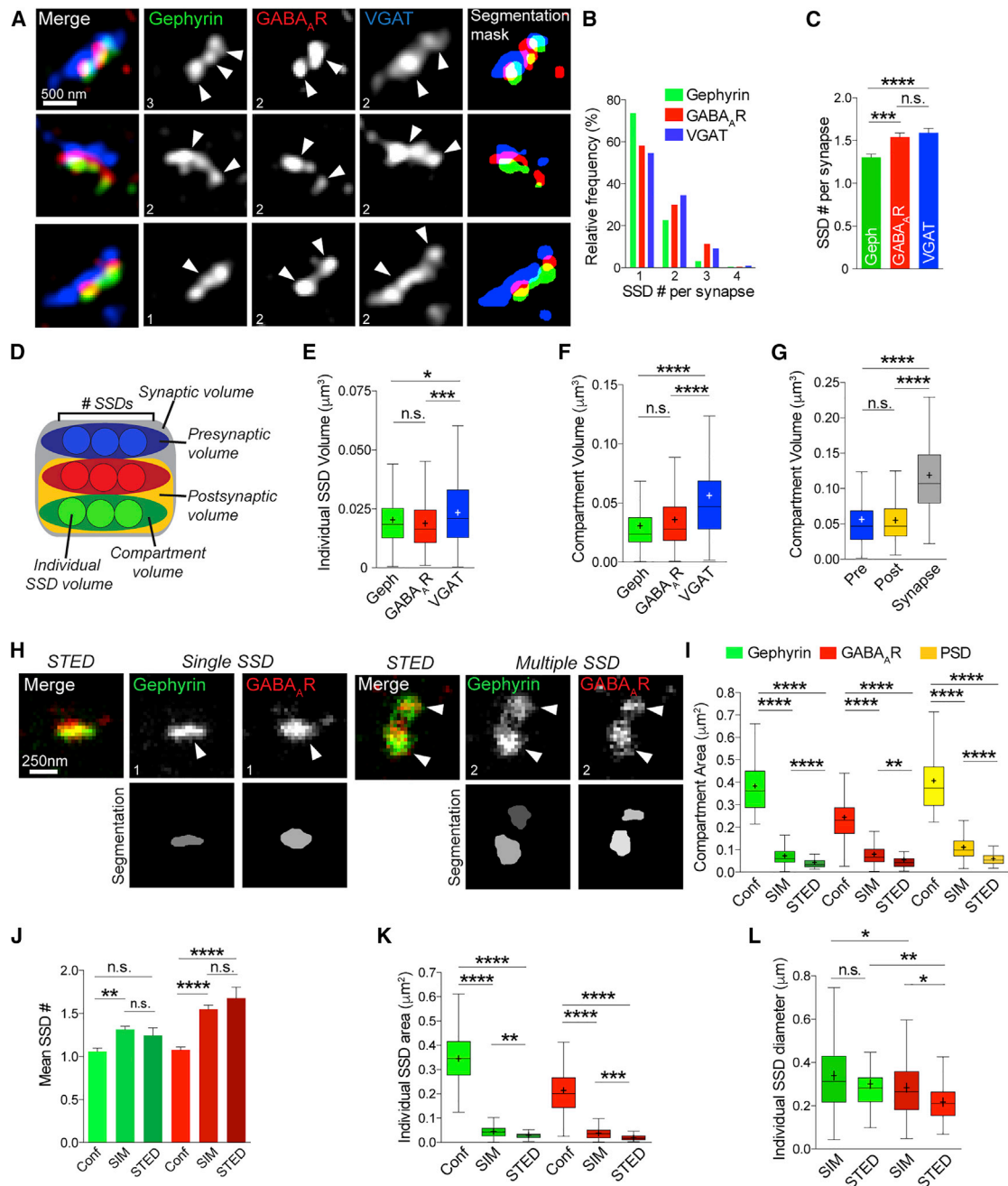
Figure 2. The Inhibitory Postsynaptic Domain Is Composed of Nanoscale SSDs

(A) Maximum projection SIM images of hippocampal inhibitory synapses and object masks generated by segmentation analysis. Numbers denote number of SSDs in compartment.

(B) Frequency distribution graph of number of SSDs per synapse for gephyrin, GABA$_A$R, and VGAT compartments.

(C) Mean number of SSDs per compartment. ****$p < 0.0001$ (Kruskal-Wallis); $n = 220$ synapses. Data are represented as mean ± SEM.

(D) Schematic of volume parameters measured by segmentation.

(E) Box plots of individual SSD volumes for gephyrin, GABA$_A$Rs, and VGAT. ****$p < 0.0001$ (Kruskal-Wallis); $n = 220$ synapses. Cross denotes mean; horizontal line denotes median.

(F) Box plots of compartment volumes for gephyrin, GABA$_A$Rs, and VGAT. ****$p < 0.0001$ (Kruskal-Wallis); $n = 220$ synapses. Cross denotes mean; horizontal line denotes median.

(G) Box plots of compartment volumes for the presynaptic site, postsynaptic site, and whole synapse ****$p < 0.0001$ (Kruskal-Wallis); $n = 220$ synapses. Cross denotes mean; horizontal line denotes median.

(H) STED images of gephyrin (green) and GABA$_A$Rs (red) from hippocampal neuronal dendrites. Numbers denote number of SSDs in compartment.

(legend continued on next page)

more SSDs that cannot be visualized by confocal microscopy (Figure 1F).

The Inhibitory Postsynaptic Domain Is Composed of Nanoscale SSDs

To identify synaptic 3D SSDs in an unbiased manner, we applied a model-based object 3D segmentation analysis (Figure S1A; Rizk et al., 2014; Shivanandan et al., 2013), which objectively produces 3D binary segmentation masks from which quantitative data can be generated in a high-throughput manner (see Figure 2A for examples). VGAT staining was used to verify functionality of the synapse and to confirm that two adjacent SSDs of $GABA_AR$ or gephyrin were part of one synapse and not two separate, juxtaposed synapses. Analysis of 220 inhibitory synapses revealed vast heterogeneity of subsynaptic structure between individual synapses (Figure 2B), with a mean number of SSDs per synapse of 1.30–1.59 and a range of 1–4 SSDs per synapse (Figure 2C). We were able to calculate volumes for each individual SSD within a synapse (individual SSD volume; Figures 2D and S1B). We could then determine the volume of each inhibitory compartment (i.e., gephyrin, $GABA_ARs$, and VGAT), the entire postsynaptic domain (PSD), and the presynaptic terminal (Figures 2D and S1B; see STAR Methods). Gephyrin and $GABA_AR$ SSDs were of similar volume, whereas the presynaptic compartment was composed of significantly larger VGAT substructures (Figure 2E). Likewise, the gephyrin and $GABA_AR$ compartments had similar volumes compared with a significantly larger VGAT compartment (Figure 2F). The volumes of the PSD and presynaptic site were almost identical, and the mean volume of the whole inhibitory synapse was approximately the size of the PSD and presynaptic site combined (Figure 2G). Notably, 3D SIM and geometric analysis of inhibitory synapses in acute slice preparations showed equivalent architectural arrangements as we observed in neuronal culture (Figures S1C and S1D).

We then compared the ability of 3D SIM to identify inhibitory postsynaptic SSDs with another super-resolution methodology, stimulated emission depletion microscopy (STED; Hell, 2009). We used two-color STED microscopy to image gephyrin and $GABA_ARs$ with ∼50 nm lateral resolution (Figure 2H). As with 3D SIM, we observed great heterogeneity in inhibitory synapse nanoscale organization between individual synapses, with synapses composed of both single and multiple SSDs (Figure 2H). As our STED images were in two dimensions, we used two-dimensional (2D) maximum projection SIM images to enable comparison between 3D SIM and 2D STED. We measured compartment area, SSD number, SSD area, and SSD diameter and compared these measurements with those obtained from STED and confocal images of gephyrin and $GABA_ARs$ (Figures

2I–2L). Both SIM and STED demonstrated improved resolution in area measurements and identification of SSDs compared with confocal microscopy (Figures 2I and 2J). Importantly, there was no difference in the number of SSDs per synaptic compartment, as identified by STED and SIM (Figure 2J), indicating that SIM provides sufficient resolution to identify inhibitory SSDs. As expected, because STED has approximately double the x-y resolution of SIM, analysis of STED images discerned slightly smaller area and diameter values than 3D SIM z projections (Figures 2K and 2L). Collectively, our SIM and STED imaging shows that the inhibitory PSD is composed of nanoscale SSDs of gephyrin scaffold and $GABA_ARs$.

Gephyrin SSDs Cluster Synaptic $GABA_AR$ SSDs

Gephyrin scaffolds $GABA_ARs$ at the inhibitory postsynaptic site (Essrich et al., 1998; Jacob et al., 2005; Kneussel et al., 1999). Although gephyrin alone has been shown to form nanoscale SSDs using PALM (Pennacchietti et al., 2017; Specht et al., 2013), the nanoscale subsynaptic relationship between gephyrin and $GABA_ARs$ has not been investigated. We hypothesized that gephyrin SSDs would cluster with $GABA_AR$ SSDs, thereby providing a mechanism for $GABA_AR$ subsynaptic organization at the inhibitory PSD. The mean individual SSD volume for gephyrin and $GABA_AR$ SSDs was very similar (Figure 3A) and was conserved within individual synapses, as determined by correlations drawn between the mean gephyrin SSD volume and the mean $GABA_AR$ volume in each synapse. This produced a significant correlation between gephyrin and $GABA_AR$ individual SSD volumes (Figure 3B) but not between gephyrin or $GABA_AR$ SSDs and VGAT substructure volumes (Figures 3C and 3D). Together, this indicates that $GABA_AR$ SSDs are of a suitable size to be clustered by gephyrin SSDs. If gephyrin SSDs do indeed cluster $GABA_AR$ SSDs, we would expect them to be closely associated within individual synapses. To determine the proximity of gephyrin and $GABA_AR$ SSDs, we calculated the fraction of 3D overlap between gephyrin and $GABA_AR$ SSDs in each synapse (Figures 3E and 3F). As expected, gephyrin and $GABA_AR$ SSD overlap was greater than overlap between gephyrin or $GABA_ARs$ with VGAT, emphasizing the ability of SIM to discern between pre- and postsynaptic sites (Figure 3G). We also found that ∼93% of all gephyrin SSDs identified overlapped with $GABA_AR$ SSDs (Figure 3H), showing that SSDs of gephyrin and $GABA_ARs$ are closely associated with each other. In synapses with multiple SSDs, gephyrin and $GABA_AR$ SSDs were often "partnered" together (as in the examples in Figure 3E), suggesting that gephyrin SSDs cluster $GABA_AR$ SSDs. We calculated the distance between neighboring gephyrin and $GABA_AR$ SSDs, revealing a mean distance of ∼140 nm, compared with the

(I) Box plots of compartment area for gephyrin, $GABA_ARs$, and PSD derived from confocal, SIM, and STED images. ****p < 0.0001 (Kruskal-Wallis); n = 54/220/37 synapses. Cross denotes mean; horizontal line denotes median.

(J) Mean number of SSDs per synapse for gephyrin and $GABA_ARs$ derived from confocal, SIM, and STED images. ****p < 0.0001 (Kruskal-Wallis); n = 54/220/37 synapses. Data are represented as mean ± SEM.

(K) Boxplots of individual SSD area for gephyrin and $GABA_ARs$ derived from confocal, SIM, and STED images. ****p < 0.0001 (Kruskal-Wallis); n = 54/220/37 synapses. Cross denotes mean; horizontal line denotes median.

(L) Boxplots of SSD diameter for gephyrin and $GABA_ARs$ derived from SIM and STED images. ****p < 0.0001 (Kruskal-Wallis); n = 54/220/37 synapses. Cross denotes mean; horizontal line denotes median.
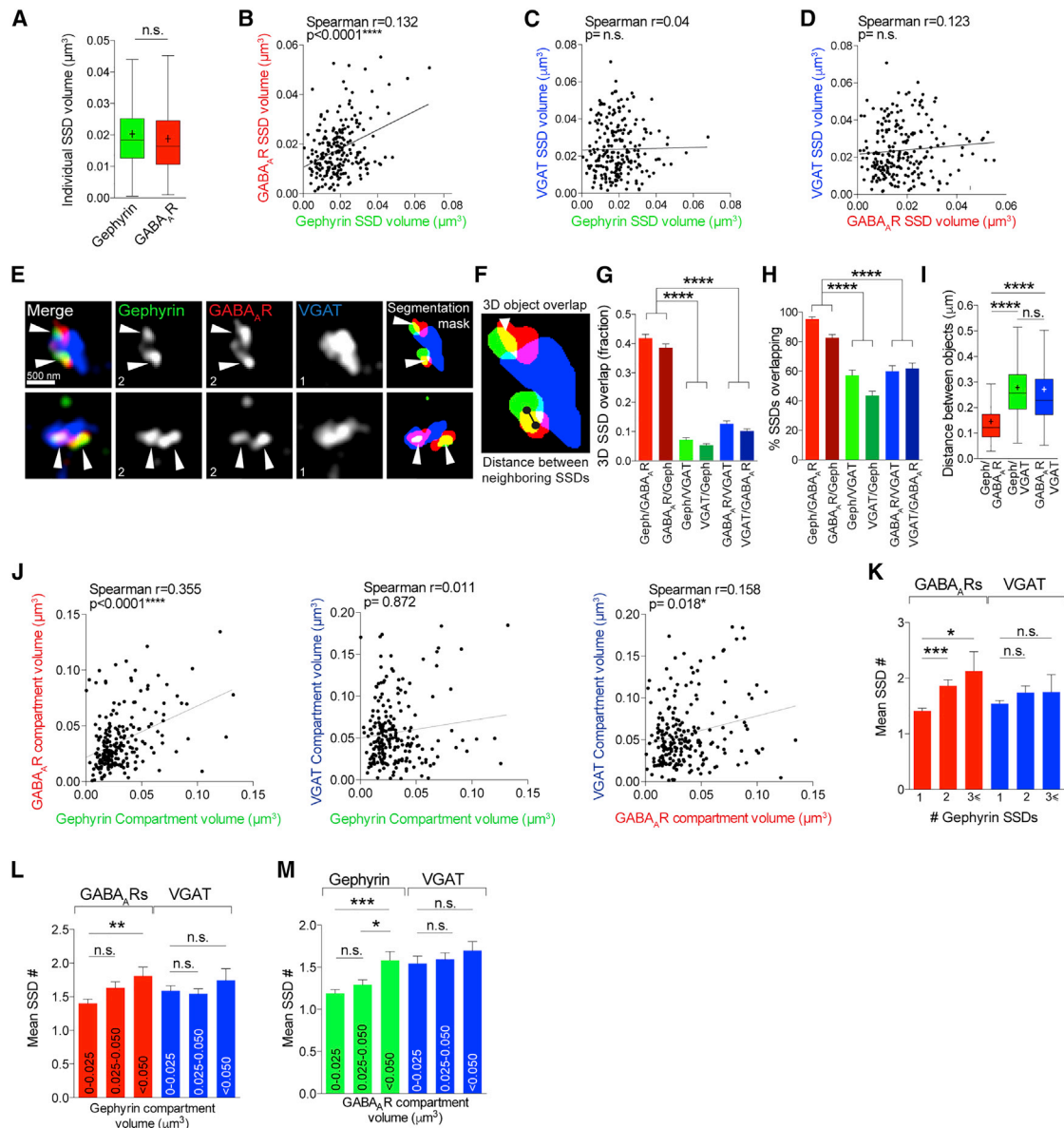
See also Figure S1.

Figure 3. Gephyrin SSDs Cluster Synaptic GABA$_A$R SSDs

(A) Boxplot comparing gephyrin and GABA$_A$R individual SSD volumes n.s. (Mann-Whitney); n = 220 synapses. Cross denotes mean; horizontal line denotes median.

(B) Correlation plot of mean GABA$_A$R SSD volume and gephyrin SSD volume per synapse. n = 220 synapses.

(C) Correlation plot of mean VGAT SSD volume and gephyrin SSD volume per synapse. n = 220 synapses.

(D) Correlation plot of mean VGAT SSD volume and GABA$_A$R SSD volume per synapse. n = 220 synapses.

(E) Maximum projection SIM images of hippocampal inhibitory synapses and object masks generated by segmentation analysis. Arrowheads point to regions of overlap between gephyrin and GABA$_A$R SSDs. Numbers denote number of SSDs in compartment.

(F) Object segmentation mask showing 3D SSD overlap and center-to-center distance between SSDs.

(G) Mean overlap fraction for gephyrin, GABA$_A$Rs, and VGAT. ****$p < 0.0001$ (Kruskal-Wallis, Dunn's post hoc); n = 220 synapses. Data are represented as mean ± SEM.

(H) Mean percentage of overlapping SSDs. ****$p < 0.0001$ (Kruskal-Wallis, Dunn's post hoc); n = 38–40 cells. Data are represented as mean ± SEM.

(I) Boxplot of center-to-center distances between neighboring SSDs. ****$p < 0.0001$ (Kruskal-Wallis, Dunn's post hoc); n = 290–340 SSDs. Cross denotes mean; horizontal line denotes median.

(J) Correlation plots of mean compartment volumes for GABA$_A$R, gephyrin, and VGAT. n = 220 synapses.

(K) Mean SSD number per GABA$_A$R or VGAT compartment for gephyrin compartments with 1, 2, or ≥3 SSDs per compartment. Gephyrin/GABA$_A$R, ****$p < 0.0001$; gephyrin/VGAT, $p = 0.236$ (Kruskal-Wallis, Dunn's post hoc); n = 220 synapses. Data are represented as mean ± SEM.

~270 nm distance between either GABA$_A$R or gephyrin SSDs with VGAT substructures (Figure 3I). Importantly, values for SSD overlap and distance between SSDs were similar when derived from acute slices (Figures S2A and S2B). We then examined how the volume of the gephyrin compartment influenced the GABA$_A$R compartment, with the view that if gephyrin SSDs cluster GABA$_A$R SSDs, there would be correlations between these compartment volumes. Correlation analysis of GABA$_A$R and VGAT compartment volumes with gephyrin compartment volumes revealed a significant similarity between gephyrin and GABA$_A$R compartment sizes, but not with VGAT compartment volume (Figure 3J), suggesting that VGAT compartment volume is likely independent of gephyrin compartment volume. We then determined whether the number of SSDs in the gephyrin compartment correlated with the number of SSDs in the GABA$_A$R compartment, thereby giving an indication of the interdependence of scaffold-receptor organization within the inhibitory PSD. Gephyrin compartments with larger numbers of SSDs were more likely to be associated with larger numbers of GABA$_A$R SSDs, but not VGAT substructures (Figure 3K). Furthermore, larger gephyrin compartments correlated with greater numbers of GABA$_A$R SSDs (Figure 3L), and larger GABA$_A$R compartments correlated with more numerous gephyrin SSDs (Figure 3M), neither with any correlation with VGAT substructure number.

To directly assess the impact of gephyrin scaffold SSD disruption on GABA$_A$R SSD organization, we expressed a dominant-negative (DN) gephyrin construct (amino acids 2–188) that interferes with gephyrin scaffold assembly (Maas et al., 2006; Sola et al., 2004) and thereby reduces GABA$_A$R clustering (Petrini et al., 2014). We used 3D SIM to image neurons expressing either the GFP-fused DN gephyrin (gephyrin-DN) or GFP as a control and stained with antibodies to endogenous gephyrin and GABA$_A$Rs (Figure 4A). Expression of gephyrin-DN caused reduced gephyrin and GABA$_A$R compartment volumes compared with control, in agreement with previous studies (Figure 4B; Maas et al., 2006; Petrini et al., 2014). However, we also observed significant reductions in both the number of gephyrin SSDs and GABA$_A$R SSDs on expression of gephyrin-DN (Figure 4C), showing that disruption of gephyrin SSDs can alter GABA$_A$R nanoscale subsynaptic clustering. This was accompanied by no change in individual SSD volume (Figure 4D) or in the correlations between gephyrin and GABA$_A$R compartment and individual SSD volumes (Figures 4E and 4F). Together, these experiments demonstrate that gephyrin and GABA$_A$R SSDs are closely associated within the inhibitory PSD and that GABA$_A$R SSD integrity is dependent on gephyrin SSD organization.

GABA$_A$R SSDs Correlate with Active-Zone RIM SSDs
At glutamatergic synapses, postsynaptic nanodomains of scaffolds and AMPARs are clustered opposite active-zone nanoclusters of the active-zone protein RIM, which defines sites of neuro-

transmitter release (Tang et al., 2016). As gephyrin and GABA$_A$R SSD number or size did not correlate with presynaptic VGAT structures, we wanted to assess whether postsynaptic inhibitory SSDs associated more accurately with structures specifically in the presynaptic active zone. Although VGAT is a reliable marker of synaptic vesicles throughout the whole inhibitory presynaptic bouton (Chaudhry et al., 1998), RIM is a precise marker of the inhibitory active zone (Kaeser et al., 2012) and regions of presynaptic neurotransmitter release (Tang et al., 2016). We first imaged synapses labeled with VGAT and RIM to determine any presence of a spatial relationship between VGAT and RIM substructures (Figure 5A). As at the excitatory synapse, we found RIM forms small discrete puncta at inhibitory axon terminals (Figure 5A), which were more numerous and significantly smaller than VGAT substructures (Figures 5B and 5C). RIM SSDs also formed compartments (representing the active zone) that were significantly smaller than VGAT compartments (Figure 5D). Although VGAT compartments were much larger, there was a strong correlation between the RIM and VGAT compartment volumes within individual synapses (Figure 5E), showing that larger VGAT-positive presynaptic terminals have larger active zones. Interestingly, we observed no correlation between RIM and VGAT individual SSD volumes in single synapses (Figure 5F), suggesting no association between the size of RIM SSDs and VGAT substructures in a given synapse. In addition, the number of SSDs of RIM and VGAT per synapse were not correlated (Figure 5G), indicating that the VGAT substructures in the presynaptic site are likely independent of the nanoscale subsynaptic organization of the active zone.

We then asked how postsynaptic gephyrin and GABA$_A$R SSDs are organized with respect to inhibitory active-zone SSDs. 3D-SIM images of synapses labeled with antibodies to gephyrin, GABA$_A$Rs, and RIM revealed that RIM SSDs form opposite the postsynaptic components of inhibitory synapses (Figure 5H). Analysis of these images revealed that the mean number of RIM SSDs per synapse was similar to that of GABA$_A$Rs and a little higher than that for gephyrin (Figure S3A). Interestingly, the compartment volume for RIM was similar to that for gephyrin or GABA$_A$Rs (Figure S3B), and this was tightly correlated within individual synapses (Figures S3C and S3D), indicating that the size of the inhibitory PSD is likely matched by a similarly sized presynaptic active zone. The mean individual SSD volume for RIM was similar to that of gephyrin and GABA$_A$R SSDs (Figure S3E). However, there was only a significant correlation across synapses between RIM and GABA$_A$R individual SSD volumes, but not gephyrin SSD volumes (Figures S3F and S3G), suggesting that the RIM SSD volume closely mirrors that of GABA$_A$Rs, but not of gephyrin SSDs. Correlation analysis between RIM SSDs and their postsynaptic counterparts showed that synapses with greater numbers of RIM SSDs also harbored larger numbers of GABA$_A$R or gephyrin SSDs (Figures 5I and 5J), pointing a close association

---

(L) Mean SSD number per GABA$_A$R or VGAT compartment for a range of gephyrin compartment volumes. Gephyrin/GABA$_A$R, **$p < 0.0073$; gephyrin/VGAT, $p = 0.755$ (Kruskal-Wallis, Dunn's post hoc); n = 220 synapses. Data are represented as mean ± SEM.

(M) Mean SSD number per gephyrin or VGAT compartment for a range of GABA$_A$R compartment volumes. GABA$_A$R/gephyrin ***$p < 0.0003$; GABA$_A$R /VGAT, $p = 0.237$ (Kruskal-Wallis, Dunn's post hoc); n = 220 synapses. Data are represented as mean ± SEM.
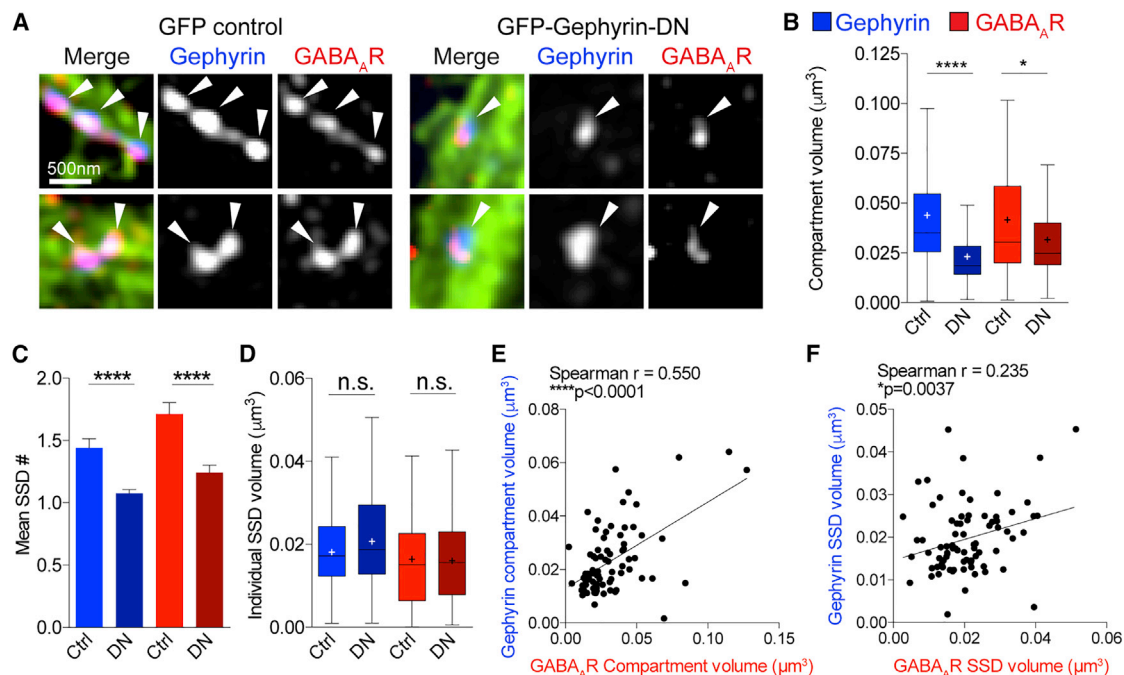
See also Figure S2.

Figure 4. Disruption of Gephyrin SSDs Reduces GABA$_A$R Nanoscale Subsynaptic Clustering

(A) Maximum projection SIM images of inhibitory synapses from GFP control and GFP-gephyrin-DN expressing hippocampal neurons. Arrowheads indicate SSDs.

(B) Boxplots of compartment volumes for gephyrin and GABA$_A$Rs in control and GFP-gephyrin-DN conditions. ****p < 0.0001 and *p < 0.020 (Mann-Whitney tests); n = 73-79 synapses. Cross denotes mean; horizontal line denotes median.

(C) Mean number of SSDs per compartment for gephyrin and GABA$_A$Rs in GFP control and GFP-gephyrin-DN conditions. ****p < 0.0001 (Mann-Whitney tests); n = 73–79 synapses. Data are represented as mean ± SEM.

(D) Boxplots of individual SSD volumes for gephyrin and GABA$_A$Rs in GFP control and GFP-gephyrin-DN conditions. n.s. (Mann-Whitney tests); n = 73–79 synapses. Cross denotes mean; horizontal line denotes median.

(E) Correlation plot of mean gephyrin compartment volume and GABA$_A$R compartment volume per synapse in GFP-gephyrin-DN neurons. n = 79 synapses.

(F) Correlation plot of mean gephyrin SSD volume and GABA$_A$R SSD volume per synapse in GFP-gephyrin-DN neurons. n = 79 synapses.

between GABA$_A$R, gephyrin and RIM SSDs. To determine whether individual RIM SSDs spatially couple with GABA$_A$R SSDs, we used proximity-based analysis to determine possible geometric association between SSDs. We determined the distance between the maximum intensity points of each RIM SSD and its nearest neighboring GABA$_A$R SSD (Figure 5K) and compared these distances with a randomized dataset derived from the same synapses, in which maximum intensity points were randomly distributed within an identical synaptic geometry (see STAR Methods for details). This comparison revealed that RIM and GABA$_A$R SSDs are significantly closer than would be observed if they were distributed randomly within a synapse (Figures 5L and 5M). After empirical inspection of the data, we defined a RIM and GABA$_A$R SSD as "paired" if they were less than 250 nm apart (Figure 5N). We classified all RIM SSDs as paired or unpaired to a neighboring GABA$_A$R SSD and found that a far greater percentage of RIM SSDs are paired to a GABA$_A$R SSD compared with the randomized dataset (Figure 5O). We then assessed whether RIM/GABA$_A$R pairs correlated with synapse volume and found that larger synapses had more RIM/GABA$_A$R pairs (Figures 5P and 5Q), suggesting that these closely associated SSDs increase in

number together as synapses get larger. Collectively, these data suggest that RIM and GABA$_A$R SSDs are similarly distributed at the inhibitory pre- and postsynaptic site, respectively, and demonstrate a close spatial relationship within the inhibitory synapse.

SSDs Are Building Blocks of the Inhibitory Postsynaptic Site

We then hypothesized that SSDs of gephyrin and GABA$_A$Rs might be building blocks for the inhibitory postsynaptic site and may represent an important mechanism for growth of this domain during plasticity. Because of the observed heterogeneity of inhibitory subsynaptic organization and synapse volumes, we first determined whether the number of SSDs within each inhibitory compartment correlated with the volume of these compartments, which would suggest that SSDs might underlie the size of the synapse during growth and potentiation. We analyzed the number of SSDs per compartment for a range of gephyrin and GABA$_A$R compartment sizes and found that the larger the compartment volume, the greater the number of SSDs within the compartment (Figure 6A). The reverse was also true: the more SSDs a compartment contained, the larger it was likely
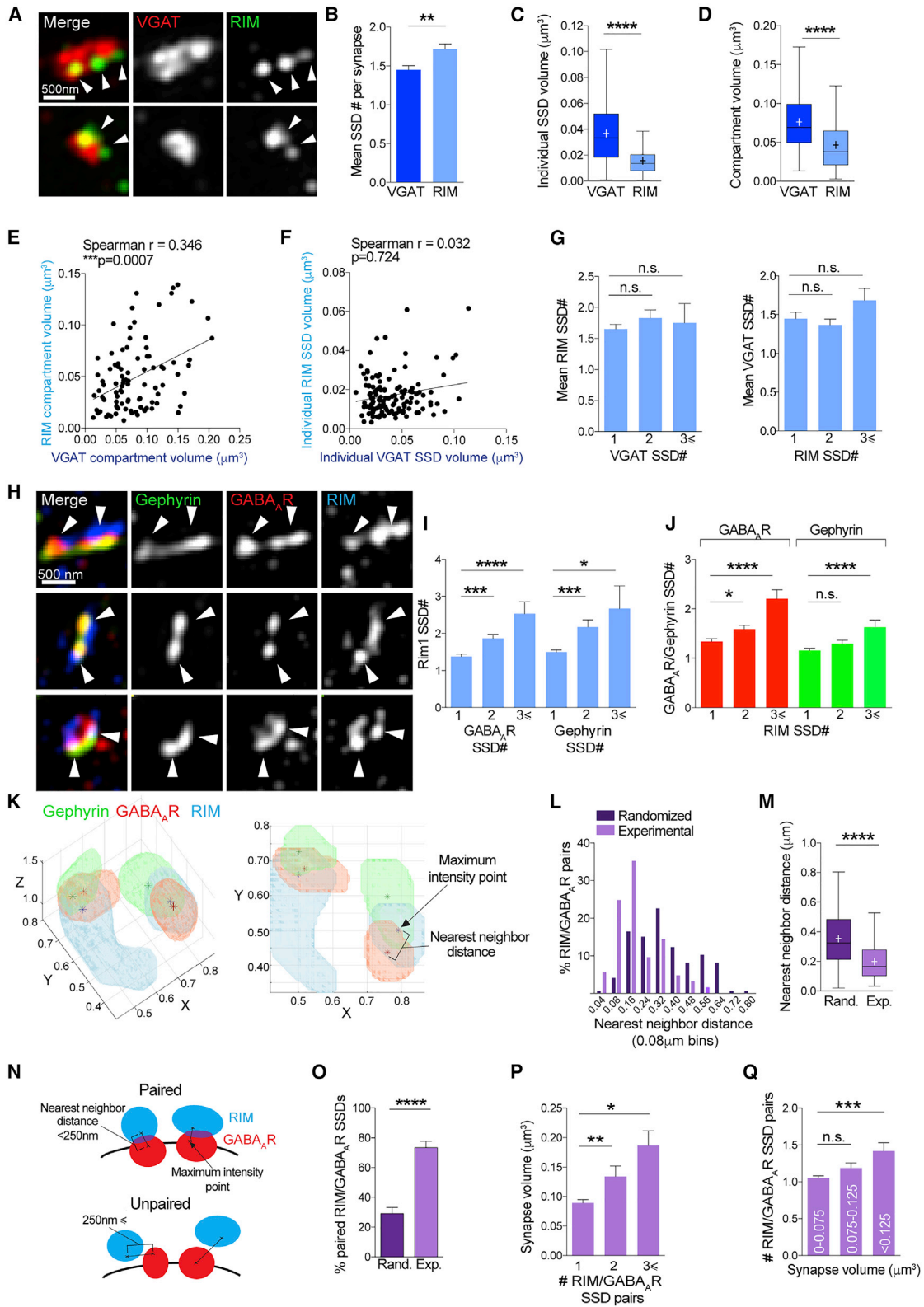
to be (Figure 6B). Furthermore, there was a strong correlation between the volume of the inhibitory PSD with the number of PSD SSDs (both gephyrin and GABA$_A$R SSDs; Figure 6C), which was also corroborated with STED imaging (Figure 6D). These data support the notion that SSDs of GABA$_A$Rs and gephyrin emerge in inhibitory synapses as they get larger. We tested this idea in the context of well-characterized homeostatic scaling protocol, which induces the growth of inhibitory synapses in conditions of excessive network activity (Peng et al., 2010; Pribiag et al., 2014; Rannals and Kapur, 2011; Ge et al., 2018). We treated neurons for 24 h with the GABA$_A$R antagonist bicuculline, to block inhibition and increase activity in the culture (Figure 6E). We observed a significant increase in the volume of the inhibitory PSD, gephyrin, and GABA$_A$R compartments at VGAT-positive synapses following bicuculline treatment (Figure 6F), which was consistent with previous studies (Peng et al., 2010; Pribiag et al., 2014). This increase in volume was accompanied by increased numbers of SSDs in each compartment, suggesting growth of inhibitory synapses during homeostatic scaling-up involves the emergence of more SSDs (Figure 6G). VGAT substructure number, volume, and compartment volume also increased with bicuculline treatment (Figures S4A–S4C). In addition, the association between gephyrin, GABA$_A$Rs, and VGAT remained constant between control and treated populations, as demonstrated by SSD overlap and nearest neighbor distance measurements (Figures S4D and S4E), suggesting that the relationship between the inhibitory synaptic components does not intrinsically change during this treatment. Intriguingly, although the number of SSDs in the synapse increased, individual SSDs did not increase in volume, and in fact they slightly reduced in size, indicating that enlargement of the synapse is not due to

individual SSDs increasing in volume but likely due to the emergence of new SSDs (Figure 6H). Furthermore, the correlation between the number of SSDs within a PSD, and its volume was preserved in the bicuculline condition (Figure 6I).

To definitively test whether SSDs arise in inhibitory synapses during synapse growth, we performed live-cell 3D SIM of hippocampal neurons expressing the GFP-gephyrin intrabody (Geph.FingR-GFP) to live-label endogenous gephyrin clusters (Gross et al., 2013). We imaged gephyrin clusters over time with control or bicuculline conditions (Figure 6J) and used segmentation analysis to determine the compartment volume and number of SSDs per synapse (Figures 6K, S4F, and S4G). In agreement with our fixed imaging experiments, the overall gephyrin compartment volume significantly increased during bicuculline treatment compared with control conditions (Figure S4F), with no increase in individual SSD volume (Figure S4G). Live 3D SIM of the same synapses over time revealed that as the gephyrin compartment became larger, more SSDs emerged (Figure 6K), thereby suggesting a role for SSD addition to the synapse in the enlargement and strengthening of inhibitory synapses during plasticity.

DISCUSSION

Using three-color 3D SIM and 3D segmentation analysis, we examined the organization and substructure of the inhibitory synapse with nanoscale resolution. We reveal that key components of the inhibitory pre- and postsynaptic sites are not homogeneous structures but are composed of nanoscale SSDs. In the PSD, gephyrin and GABA$_A$R SSDs are closely associated and demonstrate interdependence with respect to their position and

Figure 5. GABA$_A$R SSDs Correlate with Active-Zone RIM SSDs

(A) Maximum projection SIM images of VGAT and RIM-labeled inhibitory synapses.

(B) Mean number of SSDs per compartment for VGAT and RIM. **p < 0.0026 (Mann-Whitney tests); n = 127 synapses. Data are represented as mean ± SEM.

(C) Boxplot of individual SSD volumes for VGAT and RIM ****p < 0.0001 (Mann-Whitney tests); n = 127 synapses. Cross denotes mean; horizontal line denotes median.

(D) Boxplot of compartment volumes for VGAT and RIM. ****p < 0.0001 (Mann-Whitney tests); n = 127 synapses. Cross denotes mean; horizontal line denotes median.

(E) Correlation plot of VGAT compartment volume and RIM compartment volume per synapse; n = 127 synapses.

(F) Correlation plot of VGAT individual SSD volume and RIM individual SSD volume per synapse; n = 127 synapses.

(G) Mean SSD number per RIM compartment for VGAT compartments with 1, 2, or ≥3 SSDs per compartment and vice versa. n.s. (Kruskal-Wallis, Dunn's post hoc); n = 127 synapses. Data are represented as mean ± SEM.

(H) Maximum projection SIM images of gephyrin, GABA$_A$R, and RIM-labeled inhibitory synapses.

(I) Mean RIM SSD number per gephyrin or GABA$_A$R compartments with 1, 2, or ≥3 SSDs per compartment. ****p < 0.0001 (Kruskal-Wallis, Dunn's post hoc); n = 180 synapses. Data are represented as mean ± SEM.

(J) Mean GABA$_A$R or gephyrin SSD number per RIM compartments with 1, 2, or ≥3 SSDs per compartment. RIM/GABA$_A$R, ****p < 0.0001; RIM/gephyrin, p = 0.301 (Kruskal-Wallis, Dunn's post hoc); n = 180 synapses. Data are represented as mean ± SEM.

(K) 3D and 2D rendering of example inhibitory synapse with 2 SSDs of gephyrin, GABA$_A$R, and RIM (μm). Stars denote maximum intensity point within each SSD.

(L) Frequency distribution of experimental and randomized nearest neighbor distances.

(M) Boxplot of nearest neighbor distance for randomized and experimental datasets. ****p < 0.0001 (Mann-Whitney test); n = 146 RIM/GABA$_A$R SSDs. Cross denotes mean; horizontal line denotes median.

(N) Cartoon showing nearest neighbor distances between maximum intensity points within GABA$_A$R and RIM SSDs in geometrically paired and unpaired SSD synapses.

(O) Bar graph showing percentage of paired RIM and GABA$_A$R SSDs per synapse in randomized and experimental datasets. ****p < 0.0001 (Mann-Whitney test); n = 121 synapses. Data are represented as mean ± SEM.

(P). Mean volume of synapses with 1, 2, or ≥3 RIM/GABA$_A$R SSD pairs per synapse. **p < 0.0019 (Kruskal-Wallis, Dunn's post hoc); n = 121 synapses. Data are represented as mean ± SEM.

(Q) Mean number of RIM/GABA$_A$R SSD pairs per synapse for a range of synapse volumes. ***p < 0.0004 (Kruskal-Wallis, Dunn's post hoc); n = 121 synapses. Data are represented as mean ± SEM.
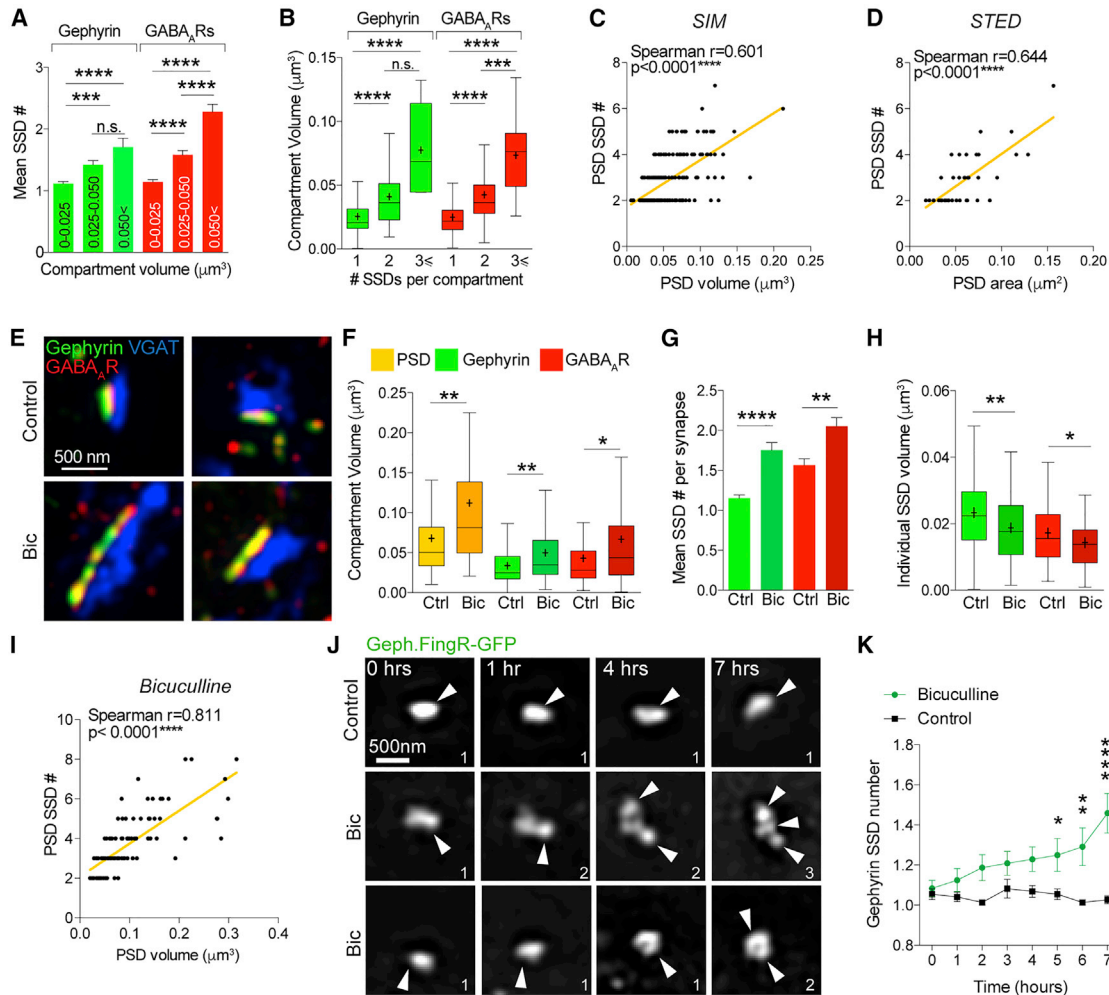
See also Figure S3.

Figure 6. SSDs Are Building Blocks of the Inhibitory Postsynaptic Domain

(A) Mean number of SSDs per compartment for a range of gephyrin and GABA$_A$R compartment sizes. ****p < 0.0001 (Kruskal-Wallis, Dunn's post hoc); n = 220 synapses. Data are represented as mean ± SEM.

(B) Mean compartment volume for gephyrin and GABA$_A$R compartments with 1, 2, or ≥3 SSDs per compartment. ****p < 0.0001 (Kruskal-Wallis, Dunn's post hoc); n = 220 synapses. Cross denotes mean; horizontal line denotes median.

(C) Correlation plot of number of PSD SSDs versus PSD volume from SIM images. n = 220 synapses.

(D) Correlation plot of number of PSD SSDs versus PSD volume from STED images. n = 37 synapses.

(E) Maximum projection SIM images of hippocampal inhibitory synapses from neurons treated with 10 μm bicuculline (Bic; 24 h) or control conditions.

(F) Boxplot of compartment volumes for PSD, gephyrin, and GABA$_A$R compartments in control and Bic conditions. PSD, **p = 0.037; gephyrin, **p = 0.0084; GABA$_A$Rs, **p = 0.0052 (Mann-Whitney); n = 85/98 synapses. Cross denotes mean; horizontal line denotes median.

(G) Mean SSD number per compartment for control and Bic conditions. Gephyrin, ****p < 0.0001; GABA$_A$Rs, **p = 0.001 (Mann-Whitney); n = 85/98 synapses. Data are represented as mean ± SEM.

(H) Boxplot of mean individual SSD volume per synapse. Gephyrin, p** < 0.0051; GABA$_A$Rs, p* = 0.040 (Mann-Whitney); n = 85/98 synapses. Cross denotes mean; horizontal line denotes median.

(I) Correlation plot of number of PSD SSDs versus PSD volume for synapses from bicuculline condition. n = 98 synapses.

(J) Maximum projection SIM images of gephyrin intrabody (Geph.FingR-GFP) acquired live in control or bicuculline treated conditions. Numbers denote number of SSDs in compartment.

(K) Graph summarizing gephyrin SSD number over time in control or Bic conditions. ****p < 0.0001 and **p < 0.01 (two-way ANOVA with Sidak's post hoc test); n = 73/48 synapses. Data are represented as mean ± SEM.

See also Figure S4.

number within individual inhibitory PSDs, suggesting that gephyrin SSDs organize GABA$_A$R SSDs. Importantly, GABA$_A$R SSDs closely associate with active-zone SSDs at inhibitory axon terminals, suggesting that the nanoscale positioning of

GABA$_A$R SSDs may be important in relation to the active zone and sites of presynaptic release. Furthermore, our live-imaging data support a model whereby postsynaptic SSDs emerge in inhibitory synapses during growth in response to changes in

network activity. Therefore, we present evidence for the architectural nanoscale organization of the inhibitory PSD, its relationship to the presynaptic active zone, and its modulation during homeostatic plasticity.

Using a high-throughput, unbiased imaging and analysis work flow, we were able to analyze hundreds of inhibitory synapses identified by GABA$_A$R, gephyrin, and VGAT/RIM immunolabeling. From this dataset we observed great heterogeneity in protein distribution patterns within the scaffold, receptor, and presynaptic compartments among individual synapses. This is in agreement with PALM and STORM imaging of glutamatergic synapses, which showed substantial variation in scaffold and neurotransmitter receptor densities across many synapses (Dani et al., 2010; MacGillavry et al., 2013). Gephyrin SSDs alone have been observed by other groups, but a similar organization of GABA$_A$Rs has only been assumed and not demonstrated (Pennacchietti et al., 2017; Specht et al., 2013). Indeed, the relationship between the nanoscale architecture of the gephyrin scaffold, GABA$_A$Rs, and proteins of inhibitory axon terminals and their behavior during plasticity in real time has not previously been studied. Here we use 3D SIM to image gephyrin along with GABA$_A$Rs and either VGAT or RIM to label inhibitory presynaptic terminals. Furthermore, we use live SIM to perform long-term imaging of gephyrin, which is impractical with other super-resolution techniques. Of the common super-resolution methods, SIM has the greatest flexibility with regard to probe selection, facilitating simultaneous imaging of three fluorophores, as well as being highly suited to live-cell imaging (Taraska, 2015). Here, we have taken advantage of these benefits, but SIM does exhibit lower resolution than both STORM-PALM and STED. We have therefore verified our results using STED imaging of GABA$_A$Rs and gephyrin, showing that SIM has a similar ability to STED regarding the identification of inhibitory SSDs. Furthermore, our measurements of inhibitory PSD area, derived from 2D SIM maximum projections, are similar to those derived from electron microscopy (Bourne and Harris, 2011; Lushnikova et al., 2011).

Our data demonstrate that gephyrin and GABA$_A$Rs are composed of nanoscale SSDs. By analyzing the distance between gephyrin and GABA$_A$R SSDs and their overlap, we find that gephyrin SSDs are enriched in synaptic GABA$_A$Rs. This is consistent with the direct interactions described between synaptic GABA$_A$R subtypes and gephyrin (Kowalczyk et al., 2013; Saiepour et al., 2010; Tretter et al., 2008) and the involvement of gephyrin in GABA$_A$R clustering (Essrich et al., 1998; Jacob et al., 2005; Kneussel et al., 1999). We show that gephyrin and GABA$_A$R SSDs are of similar volume and closely associated. There are significant correlations between GABA$_A$R and gephyrin compartment volumes and the numbers of SSDs they contain, suggesting interdependence between the SSDs of the receptor and scaffold in the inhibitory PSD. Moreover, disruption of the gephyrin scaffold with a DN gephyrin construct reduces both gephyrin and GABA$_A$R compartment volume but also the number of SSDs per compartment, demonstrating a direct role for gephyrin SSDs in the nanoscale organization of GABA$_A$Rs in the inhibitory PSD. In addition to gephyrin, numerous other inhibitory postsynaptic proteins participate in GABA$_A$R stabilization at synapses and therefore represent prime candidates to contribute to the

subsynaptic positioning of GABA$_A$Rs at the postsynaptic site. These include the accessory protein LHFPL4/GARLH (Davenport et al., 2017; Yamasaki et al., 2017) and the scaffold GIT1 (Smith et al., 2014a), both of which are essential for correct synaptic GABA$_A$R clustering and stability. In addition, gephyrin clustering is regulated by post-translational modifications such as phosphorylation and palmitoylation (Dejanovic et al., 2014; Herweg and Schwarz, 2012; Tyagarajan et al., 2011, 2013), which would also likely alter the subsynaptic nanoscale organization of both gephyrin and GABA$_A$Rs. Going forward, it will be essential to determine the roles of such interacting proteins and post-translational modifications in the nanoscale subsynaptic organization of the inhibitory synapse and how this is modulated in synaptic plasticity.

The interdependence between GABA$_A$R SSDs and their scaffold is in stark contrast to the minimal association observed with presynaptic VGAT substructures. This discordance is likely due to VGAT labeling the whole population of synaptic vesicles in the axon terminal (Chaudhry et al., 1998) rather than a specific presynaptic functional domain, such as the active zone. Although we can identify substructure in the VGAT labeling, these substructures are significantly larger than both GABA$_A$R and gephyrin SSDs and exhibit no correlations with the postsynaptic nanoscale organization. To verify whether VGAT substructures are linked to the active zone, we imaged VGAT and the active-zone protein RIM, which labels neurotransmitter release sites (Tang et al., 2016) and, we show, forms punctate nanoscale SSDs in the inhibitory axon terminal. Our analysis revealed that VGAT substructures are substantially larger than RIM SSDs, and there is no correlation between VGAT and RIM structures with respect to both the number and the size of the substructures within single synapses. This suggests that VGAT substructures are not spatially linked to the smaller and more numerous RIM SSDs in the inhibitory presynaptic domain and are not representative of the active zone.

As VGAT substructures were not associated with gephyrin and GABA$_A$R SSDs, we imaged gephyrin, GABA$_A$Rs, and RIM to assess whether the inhibitory postsynaptic SSDs were spatially linked to the organization of the active zone and presynaptic release sites. We found that RIM SSDs were of similar size and number as GABA$_A$R SSDs located in the PSD, suggesting that presynaptic release sites in the inhibitory active zone could be linked to postsynaptic GABA$_A$R clustering. Importantly, there were strong correlations between the numbers of GABA$_A$R and gephyrin SSDs and presynaptic RIM SSDs in individual synapses, pointing to a potential association between pre- and postsynaptic SSDs. Indeed, further analysis of RIM and GABA$_A$R SSDs showed that these SSDs are closely associated within the inhibitory synapse, suggesting that GABA$_A$R SSDs are spatially linked to presynaptic sites of release in the inhibitory active zone. Like AMPARs at excitatory synapses, the subsynaptic clustering of GABA$_A$Rs in close proximity to GABA release sites is likely crucial for synaptic transmission because of the similarities between glutamate and GABA release and their binding to AMPA and GABA$_A$Rs, respectively. First, on release into the synaptic cleft, GABA has a very similar spatial and temporal profile to that of glutamate: it reaches high concentrations in the vicinity of the release site, which

decreases rapidly over time (Clements, 1996; Mozrzymas et al., 2003) and with increasing distance from the release site (Petrini et al., 2011). Second, like the behavior of AMPARs, during quantal GABA release GABA$_A$Rs are not thought to become saturated (Frerking et al., 1995; Perrais and Ropert, 1999) and only a fraction of the receptors at the synapse are activated (Edwards et al., 1990). This would therefore suggest that subsynaptic positioning of the receptors near a GABA release site would be imperative for shaping the postsynaptic response to that event and may provide a way to alter synaptic strength during plasticity.

Using fixed and live-cell 3D SIM, we show that SSDs emerge in the inhibitory PSD during growth, suggesting that SSDs are building blocks for synaptic architecture and provide a mechanism by which synapse growth may occur. Importantly, during a long-term homeostatic scaling treatment shown to cause inhibitory synapse growth (Peng et al., 2010; Pribiag et al., 2014), we show that increased compartment volume is accompanied by greater numbers of PSD SSDs. This is supported by live 3D SIM experiments showing that SSDs emerge in gephyrin compartments as they enlarge over time due to increased network activity. Importantly, individual SSDs do not increase in volume during this scaling, indicating that SSDs are likely added to the synapse as it gets larger, rather than existing SSDs expanding to grow the synapse. Together, these experiments indicate that inhibitory postsynaptic SSDs likely work in concert to enlarge the synapse in response to excessive neuronal activity. Key questions now remain as to the details of how this process works, whether gephyrin and GABA$_A$R SSDs are added together or separately, and whether this mechanism of synapse growth is common to different types of inhibitory potentiation.

Here, we have presented a common nanoscale architecture for inhibitory synapses located on dendrites of cultured hippocampal neurons. There is, of course, great variability of synaptic structure and function across the brain and even within the same neuron. Indeed, our data here show great variation in the nanoscale architecture of dendritic inhibitory synapses. Thus, in future studies it will be paramount to determine whether these nanoscale properties are applicable to all types of inhibitory synapses or differ between subcellular location (e.g., somatic versus dendritic), type of innervating interneuron, and brain region.

STAR★METHODS

Detailed methods are provided in the online version of this paper and include the following:

- KEY RESOURCES TABLE
- CONTACT FOR REAGENT AND RESOURCE SHARING
- EXPERIMENTAL MODEL AND SUBJECT DETAILS
- DISSOCIATED HIPPOCAMPAL CULTURES AND ACUTE CORTICAL SLICE PREPARATION
- METHOD DETAILS
  - Immunofluorescence
  - Microscopy
  - Image analysis
- QUANTIFICATION AND STATISTICAL ANALYSIS

AUTHOR CONTRIBUTIONS

Conceptualization, K.R.S.; Software, K.C.C.; Formal Analysis and Investigation, K.C.C., S.E.G., J.D.G., K.M.H., and K.R.S.; Methodology, K.R.S. and K.C.C.; Writing – Original Draft, K.R.S.; Writing – Review & Editing, K.R.S., K.C.C., and M.L.D.; Supervision, K.R.S. and M.L.D.; Funding Acquisition, K.R.S. and M.L.D.

DECLARATION OF INTERESTS

The authors declare no competing interests.

REFERENCES

Ball, G., Demmerle, J., Kaufmann, R., Davis, I., Dobbie, I.M., and Schermelleh, L. (2015). SIMcheck: a toolbox for successful super-resolution structured illumination microscopy. Sci. Rep. 5, 15915.

Biederer, T., Kaeser, P.S., and Blanpied, T.A. (2017). Transcellular nanoalignment of synaptic function. Neuron 96, 680–696.

Blundell, J., Tabuchi, K., Bolliger, M.F., Blaiss, C.A., Brose, N., Liu, X., Südhof, T.C., and Powell, C.M. (2009). Increased anxiety-like behavior in mice lacking the inhibitory synapse cell adhesion molecule neuroligin 2. Genes Brain Behav. 8, 114–126.

Bourne, J.N., and Harris, K.M. (2011). Coordination of size and number of excitatory and inhibitory synapses results in a balanced structural plasticity along mature hippocampal CA1 dendrites during LTP. Hippocampus 21, 354–373.

Bowen, A.B., Bourke, A.M., Hiester, B.G., Hanus, C., and Kennedy, M.J. (2017). Golgi-independent secretory trafficking through recycling endosomes in neuronal dendrites and spines. eLife 6, e27362.

Chaudhry, F.A., Reimer, R.J., Bellocchio, E.E., Danbolt, N.C., Osen, K.K., Edwards, R.H., and Storm-Mathisen, J. (1998). The vesicular GABA transporter, VGAT, localizes to synaptic vesicles in sets of glycinergic as well as GABAergic neurons. J. Neurosci. 18, 9733–9750.

Chen, H., Tang, A.H., and Blanpied, T.A. (2018). Subsynaptic spatial organization as a regulator of synaptic strength and plasticity. Curr. Opin. Neurobiol. 51, 147–153.

Clements, J.D. (1996). Transmitter timecourse in the synaptic cleft: its role in central synaptic function. Trends Neurosci. *19*, 163–171.

Dani, A., Huang, B., Bergan, J., Dulac, C., and Zhuang, X. (2010). Superresolution imaging of chemical synapses in the brain. Neuron *68*, 843–856.

Davenport, E.C., Pendolino, V., Kontou, G., McGee, T.P., Sheehan, D.F., López-Doménech, G., Farrant, M., and Kittler, J.T. (2017). An essential role for the tetraspanin LHFPL4 in the cell-type-specific targeting and clustering of synaptic GABA$_A$ receptors. Cell Rep. *21*, 70–83.

Dejanovic, B., Semtner, M., Ebert, S., Lamkemeyer, T., Neuser, F., Lüscher, B., Meier, J.C., and Schwarz, G. (2014). Palmitoylation of gephyrin controls receptor clustering and plasticity of GABAergic synapses. PLoS Biol. *12*, e1001908.

Edwards, F.A., Konnerth, A., and Sakmann, B. (1990). Quantal analysis of inhibitory synaptic transmission in the dentate gyrus of rat hippocampal slices: a patch-clamp study. J. Physiol. *430*, 213–249.

Essrich, C., Lorez, M., Benson, J.A., Fritschy, J.-M., and Lüscher, B. (1998). Postsynaptic clustering of major GABAA receptor subtypes requires the gamma 2 subunit and gephyrin. Nat. Neurosci. *1*, 563–571.

Flores, C.E., and Méndez, P. (2014). Shaping inhibition: activity dependent structural plasticity of GABAergic synapses. Front. Cell. Neurosci. *8*, 327.

Frerking, M., Borges, S., and Wilson, M. (1995). Variation in GABA mini amplitude is the consequence of variation in transmitter concentration. Neuron *15*, 885–895.

Fukata, Y., Dimitrov, A., Boncompain, G., Vielemeyer, O., Perez, F., and Fukata, M. (2013). Local palmitoylation cycles define activity-regulated postsynaptic subdomains. J. Cell Biol. *202*, 145–161.

Ge, Y., Kang, Y., Cassidy, R.M., Moon, K.M., Lewis, R., Wong, R.O.L., Foster, L.J., and Craig, A.M. (2018). Clptm1 limits forward trafficking of GABAA receptors to scale inhibitory synaptic strength. Neuron *97*, 596–610.e8.

Gross, G.G., Junge, J.A., Mora, R.J., Kwon, H.B., Olson, C.A., Takahashi, T.T., Liman, E.R., Ellis-Davies, G.C., McGee, A.W., Sabatini, B.L., et al. (2013). Recombinant probes for visualizing endogenous synaptic proteins in living neurons. Neuron *78*, 971–985.

Haas, K.T., Compans, B., Letellier, M., Bartol, T.M., Grillo-Bosch, D., Sejnowski, T.J., Sainlos, M., Choquet, D., Thoumine, O., and Hosy, E. (2018). Pre-post synaptic alignment through neuroligin-1 tunes synaptic transmission efficiency. eLife *7*, e31755.

Hedrick, T., and Waters, J. (2010). Physiological properties of cholinergic and non-cholinergic magnocellular neurons in acute slices from adult mouse nucleus basalis. PLoS ONE *5*, e11046.

Hell, S.W. (2009). Microscopy and its focal switch. Nat. Methods *6*, 24–32.

Herweg, J., and Schwarz, G. (2012). Splice-specific glycine receptor binding, folding, and phosphorylation of the scaffolding protein gephyrin. J. Biol. Chem. *287*, 12645–12656.

Hruska, M., Henderson, N., Le Marchand, S.J., Jafri, H., and Dalva, M.B. (2018). Synaptic nanomodules underlie the organization and plasticity of spine synapses. Nat. Neurosci. *21*, 671–682.

Jacob, T., Bogdanov, Y., Magnus, C., Saliba, R., Kittler, J., Haydon, P., and Moss, S. (2005). Gephyrin regulates the cell surface dynamics of synaptic GABAA receptors. J. Neurosci. *25*, 10469–10478.

Kaeser, P.S., Deng, L., Fan, M., and Südhof, T.C. (2012). RIM genes differentially contribute to organizing presynaptic release sites. Proc. Natl. Acad. Sci. U S A *109*, 11830–11835.

Klausberger, T., and Somogyi, P. (2008). Neuronal diversity and temporal dynamics: the unity of hippocampal circuit operations. Science *321*, 53–57.

Kneussel, M., Brandstatter, J., Laube, B., Stahl, S., Muller, U., and Betz, H. (1999). Loss of postsynaptic GABA(A) receptor clustering in gephyrin-deficient mice. J. Neurosci. *19*, 9289–9297.

Kowalczyk, S., Winkelmann, A., Smolinsky, B., Förstera, B., Neundorf, I., Schwarz, G., and Meier, J.C. (2013). Direct binding of GABAA receptor β2 and β3 subunits to gephyrin. Eur. J. Neurosci. *37*, 544–554.

Luscher, B., Fuchs, T., and Kilpatrick, C.L. (2011). GABAA receptor trafficking-mediated plasticity of inhibitory synapses. Neuron *70*, 385–409.

Lushnikova, I., Skibo, G., Muller, D., and Nikonenko, I. (2011). Excitatory synaptic activity is associated with a rapid structural plasticity of inhibitory synapses on hippocampal CA1 pyramidal cells. Neuropharmacology *60*, 757–764.

Maas, C., Tagnaouti, N., Loebrich, S., Behrend, B., Lappe-Siefke, C., and Kneussel, M. (2006). Neuronal cotransport of glycine receptor and the scaffold protein gephyrin. J. Cell Biol. *172*, 441–451.

MacGillavry, H.D., and Hoogenraad, C.C. (2015). The internal architecture of dendritic spines revealed by super-resolution imaging: what did we learn so far? Exp. Cell Res. *335*, 180–186.

MacGillavry, H.D., Song, Y., Raghavachari, S., and Blanpied, T.A. (2013). Nanoscale scaffolding domains within the postsynaptic density concentrate synaptic AMPA receptors. Neuron *78*, 615–622.

Meyer, S.A., Ozbay, B.N., Potcoava, M., Salcedo, E., Restrepo, D., and Gibson, E.A. (2016). Super-resolution imaging of ciliary microdomains in isolated olfactory sensory neurons using a custom two-color stimulated emission depletion microscope. J. Biomed. Opt. *21*, 66017.

Mozrzymas, J.W., Zarnowska, E.D., Pytel, M., and Mercik, K. (2003). Modulation of GABA(A) receptors by hydrogen ions reveals synaptic GABA transient and a crucial role of the desensitization process. J. Neurosci. *23*, 7981–7992.

Nair, D., Hosy, E., Petersen, J.D., Constals, A., Giannone, G., Choquet, D., and Sibarita, J.B. (2013). Super-resolution imaging reveals that AMPA receptors inside synapses are dynamically organized in nanodomains regulated by PSD95. J. Neurosci. *33*, 13204–13224.

Nusser, Z., Hájos, N., Somogyi, P., and Mody, I. (1998). Increased number of synaptic GABA(A) receptors underlies potentiation at hippocampal inhibitory synapses. Nature *395*, 172–177.

Papadopoulos, T., Korte, M., Eulenburg, V., Kubota, H., Retiounskaia, M., Harvey, R.J., Harvey, K., O'Sullivan, G.A., Laube, B., Hülsmann, S., et al. (2007). Impaired GABAergic transmission and altered hippocampal synaptic plasticity in collybistin-deficient mice. EMBO J. *26*, 3888–3899.

Paul, G., Cardinale, J., and Sbalzarini, I. (2013). Coupling image restoration and segmentation: a generalized linear model/Bregman perspective. Int. J. Comput. Vis. *104*, 69–93.

Peng, Y.R., Zeng, S.Y., Song, H.L., Li, M.Y., Yamada, M.K., and Yu, X. (2010). Postsynaptic spiking homeostatically induces cell-autonomous regulation of inhibitory inputs via retrograde signaling. J. Neurosci. *30*, 16220–16231.

Pennacchietti, F., Vascon, S., Nieus, T., Rosillo, C., Das, S., Tyagarajan, S.K., Diaspro, A., Del Bue, A., Petrini, E.M., Barberis, A., and Cella Zanacchi, F. (2017). Nanoscale molecular reorganization of the inhibitory postsynaptic density is a determinant of GABAergic synaptic potentiation. J. Neurosci. *37*, 1747–1756.

Perrais, D., and Ropert, N. (1999). Effect of zolpidem on miniature IPSCs and occupancy of postsynaptic GABAA receptors in central synapses. J. Neurosci. *19*, 578–588.

Petrini, E.M., and Barberis, A. (2014). Diffusion dynamics of synaptic molecules during inhibitory postsynaptic plasticity. Front. Cell. Neurosci. *8*, 300.

Petrini, E.M., Nieus, T., Ravasenga, T., Succol, F., Guazzi, S., Benfenati, F., and Barberis, A. (2011). Influence of GABAAR monoliganded states on GABAergic responses. J. Neurosci. *31*, 1752–1761.

Petrini, E.M., Ravasenga, T., Hausrat, T.J., Iurilli, G., Olcese, U., Racine, V., Sibarita, J.B., Jacob, T.C., Moss, S.J., Benfenati, F., et al. (2014). Synaptic recruitment of gephyrin regulates surface GABAA receptor dynamics for the expression of inhibitory LTP. Nat. Commun. *5*, 3921.

Pribiag, H., Peng, H., Shah, W.A., Stellwagen, D., and Carbonetto, S. (2014). Dystroglycan mediates homeostatic synaptic plasticity at GABAergic synapses. Proc. Natl. Acad. Sci. USA *111*, 6810–6815.

Purkey, A.M., Woolfrey, K.M., Crosby, K.C., Stich, D.G., Chick, W.S., Aoto, J., and Dell'Acqua, M.L. (2018). AKAP150 palmitoylation regulates synaptic incorporation of Ca(2+)-permeable AMPA receptors to control LTP. Cell Rep. *25*, 974–987.e4.

Rannals, M.D., and Kapur, J. (2011). Homeostatic strengthening of inhibitory synapses is mediated by the accumulation of GABA(A) receptors. J. Neurosci. *31*, 17701–17712.

Rizk, A., Paul, G., Incardona, P., Bugarski, M., Mansouri, M., Niemann, A., Ziegler, U., Berger, P., and Sbalzarini, I.F. (2014). Segmentation and quantification of subcellular structures in fluorescence microscopy images using Squassh. Nat. Protoc. *9*, 586–596.

Saiepour, L., Fuchs, C., Patrizi, A., Sassoe-Pognetto, M., Harvey, R.J., and Harvey, K. (2010). The complex role of collybistin and gephyrin in GABAA receptor clustering. J. Biol. Chem. *285*, 29623–29631.

Shivanandan, A., Radenovic, A., and Sbalzarini, I.F. (2013). MosaicIA: an ImageJ/Fiji plugin for spatial pattern and interaction analysis. BMC Bioinformatics *14*, 349.

Sinnen, B.L., Bowen, A.B., Forte, J.S., Hiester, B.G., Crosby, K.C., Gibson, E.S., Dell'Acqua, M.L., and Kennedy, M.J. (2017). Optogenetic control of synaptic composition and function. Neuron *93*, 646–660.e5.

Smith, K.R., and Kittler, J.T. (2010). The cell biology of synaptic inhibition in health and disease. Curr. Opin. Neurobiol. *20*, 550–556.

Smith, K.R., Davenport, E.C., Wei, J., Li, X., Pathania, M., Vaccaro, V., Yan, Z., and Kittler, J.T. (2014a). GIT1 and βPIX are essential for GABA(A) receptor synaptic stability and inhibitory neurotransmission. Cell Rep. *9*, 298–310.

Smith, K.R., Kopeikina, K.J., Fawcett-Patel, J.M., Leaderbrand, K., Gao, R., Schürmann, B., Myczek, K., Radulovic, J., Swanson, G.T., and Penzes, P. (2014b). Psychiatric risk factor ANK3/ankyrin-G nanodomains regulate the structure and function of glutamatergic synapses. Neuron *84*, 399–415.

Sola, M., Bavro, V.N., Timmins, J., Franz, T., Ricard-Blum, S., Schoehn, G., Ruigrok, R.W., Paarmann, I., Saiyed, T., O'Sullivan, G.A., et al. (2004). Structural basis of dynamic glycine receptor clustering by gephyrin. EMBO J. *23*, 2510–2519.

Specht, C.G., Izeddin, I., Rodriguez, P.C., El Beheiry, M., Rostaing, P., Darzacq, X., Dahan, M., and Triller, A. (2013). Quantitative nanoscopy of inhibitory synapses: counting gephyrin molecules and receptor binding sites. Neuron *79*, 308–321.

Tang, A.H., Chen, H., Li, T.P., Metzbower, S.R., MacGillavry, H.D., and Blanpied, T.A. (2016). A trans-synaptic nanocolumn aligns neurotransmitter release to receptors. Nature *536*, 210–214.

Taraska, J.W. (2015). SIMply better resolution in live cells. Trends Cell Biol. *25*, 636–638.

Tønnesen, J., Katona, G., Rózsa, B., and Nägerl, U.V. (2014). Spine neck plasticity regulates compartmentalization of synapses. Nat. Neurosci. *17*, 678–685.

Tretter, V., Jacob, T., Mukherjee, J., Fritschy, J., Pangalos, M., and Moss, S. (2008). The clustering of GABA(A) receptor subtypes at inhibitory synapses is facilitated via the direct binding of receptor alpha 2 subunits to gephyrin. J. Neurosci. *28*, 1356–1365.

Tretter, V., Revilla-Sanchez, R., Houston, C., Terunuma, M., Havekes, R., Florian, C., Jurd, R., Vithlani, M., Michels, G., Couve, A., et al. (2009). Deficits in spatial memory correlate with modified gamma-aminobutyric acid type A receptor tyrosine phosphorylation in the hippocampus. Proc. Natl. Acad. Sci. U S A *106*, 20039–20044.

Tyagarajan, S.K., Ghosh, H., Yévenes, G.E., Nikonenko, I., Ebeling, C., Schwerdel, C., Sidler, C., Zeilhofer, H.U., Gerrits, B., Muller, D., and Fritschy, J.M. (2011). Regulation of GABAergic synapse formation and plasticity by GSK3beta-dependent phosphorylation of gephyrin. Proc. Natl. Acad. Sci. U S A *108*, 379–384.

Tyagarajan, S.K., Ghosh, H., Yévenes, G.E., Imanishi, S.Y., Zeilhofer, H.U., Gerrits, B., and Fritschy, J.M. (2013). Extracellular signal-regulated kinase and glycogen synthase kinase 3β regulate gephyrin postsynaptic aggregation and GABAergic synaptic function in a calpain-dependent mechanism. J. Biol. Chem. *288*, 9634–9647.

Yamasaki, T., Hoyos-Ramirez, E., Martenson, J.S., Morimoto-Tomita, M., and Tomita, S. (2017). GARLH family proteins stabilize GABAA receptors at synapses. Neuron *93*, 1138–1152.e6.

Yizhar, O., Fenno, L.E., Prigge, M., Schneider, F., Davidson, T.J., O'Shea, D.J., Sohal, V.S., Goshen, I., Finkelstein, J., Paz, J.T., et al. (2011). Neocortical excitation/inhibition balance in information processing and social dysfunction. Nature *477*, 171–178.

STAR★METHODS

KEY RESOURCES TABLE

REAGENT or RESOURCE	SOURCE	IDENTIFIER
Antibodies		
Polyclonal guinea pig γ2-GABA$_A$R	Synaptic systems	Cat# 224004; RRID: AB_10594245
Monoclonal mouse anti-gephyrin	Synaptic systems	Cat# 147011; RRID: AB_887717
Polyclonal rabbit VGAT	Synaptic systems	Cat# 131003; RRID: AB_887869
Polyclonal rabbit RIM1/2	Synaptic systems	Cat# 140203; RRID: AB_887775
STAR 580 Goat anti-guinea pig	Abberior	Cat#: 2-0112-005-7
STAR 635 Goat anti-mouse	Abberior	Cat#: 2-0002-002-0
Goat anti-guinea pig Alexa Fluor-568	Life Technologies	Cat# A11075; RRID: 141954
Donkey anti-mouse AlexaFluor-488	Life Technologies	Cat# A21202; RRID: 141607
Donkey anti-rabbit Alexa Fluor-647	Life Technologies	Cat# A31573; RRID: 2536183
Chemicals, Peptides, and Recombinant Proteins		
(-)-Bicuculline methiodide	Tocris	Cat# 2503
Experimental Models: Organisms/Strains		
Rat, Sprague Dawley Charles River	Charles Rivers	Crl:CD(SD)BR; RRID: RGD_734476
C57BL/6J mice	Jackson Laboratories	IMSR_JAX:000664
Recombinant DNA		
Gephyrin FingR	Gross et al., 2013	Addgene # 46296
Software and Algorithms		
ImageJ	National Institutes of Health	https://imagej.nih.gov/ij/
NIS Elements	Nikon	https://www.nikoninstruments.com/Products/Software
Prism	GraphPad	https://www.graphpad.com/scientific-software/prism/
Mosaic Suite (FIJI/ImageJ plugin)	Mosaic Group	http://mosaic.mpi-cbg.de/?q=downloads/imageJ
MATLAB	Mathworks	http://www.mathworks.com

CONTACT FOR REAGENT AND RESOURCE SHARING

Information about and requests for reagents and resources should be directed to and will be fulfilled by the Lead Contact, Katharine Smith (katharine.r.smith@ucdenver.edu).

EXPERIMENTAL MODEL AND SUBJECT DETAILS

All animal procedures were conducted in accordance with National Institutes of Health (NIH)–United States Public Health Service guidelines and with the approval of the University of Colorado, Denver, Institutional Animal Care and Use Committee.

DISSOCIATED HIPPOCAMPAL CULTURES AND ACUTE CORTICAL SLICE PREPARATION

Rat hippocampal neurons were cultured from postnatal day 1–2 mixed sex rats as previously described (Bowen et al., 2017). Briefly, the hippocampus was dissected from postnatal day 1-2 rats and dissociated in papain. Neurons were seeded at a density of 150,000-200,000 cells on 18mm glass #1.5 coverslips coated with poly-D-lysine. Cells were maintained at 37°C, 5% CO2 for 14–16 days before fixation. For live imaging, dissociated hippocampal neurons were transfected with 400ng of Gephyrin-FingR DNA at 14-15 DIV, using Lipofectamine2000 according to the manufacturer's protocol. To generate acute slices, 4-5 week old mice were perfused as described in (Hedrick and Waters, 2010) and 30 μm slices were cut from cortex.

METHOD DETAILS

Immunofluorescence

Neurons were washed with 1XPBS, then fixed in 4% paraformaldehyde/4% sucrose in 1XPBS for 5 minutes. After 3 washes with 1XPBS, the neurons were blocked for 1 hour in a non-permeabilizing block solution (5% BSA, 2% normal goat serum in 1XPBS). Neurons were then incubated with anti- γ2-GABA$_A$R antibody (1:400; Synaptic Systems) in non-permeabilizing block solution for 1 hour at RT. Neurons were then washed in 1XPBS and permeabilized in permeabilizing block solution (5% BSA, 2% normal goat serum, 0.2% Triton X-100, in 1XPBS) for 10 minutes. Neurons were then incubated with antibodies to gephyrin (1:400) and VGAT or RIM (1:1000; both Synaptic Systems) in block solution for 1 hour at RT. After washing with 1XPBS, neurons were then incubated with secondary antibody conjugated to fluorescent proteins for 1 hour at RT. Coverslips were washed in 1XPBS and mounted onto glass slides with Pro-Long Gold (Invitrogen). For immunohistochemistry, cortical slices were stained as previously described (Hedrick and Waters, 2010) using the anti-γ2-GABA$_A$R and gephyrin antibodies at 1:700, and the VGAT antibody at 1:1000.

Microscopy

SIM

Multichannel SIM images were acquired using a Nikon SIM-E Structured Illumination super-resolution microscope with a 100x 1.49 NA objective in a similar manner to (Smith et al., 2014b). Samples were excited with illumination from 488, 561, and 640 laser diodes. Emission light was detected by an ORCA-Flash 4.0 sCMOS camera (Hamamatsu). Acquisition conditions were adjusted to optimize for a high signal to noise ratio (> 8), reduce photobleaching, and to keep the overall count-level below 12000. Camera integration time was kept between 100-300ms. For each coverslip imaged, the correction collar was adjusted automatically and an FT image was used to confirm optimal correction collar position. For 3D-stack reconstruction, the illumination modulation contrast was set automatically by the software (Nikon Elements) and the high-resolution noise suppression was set to 1. These parameters were kept consistent across all acquisitions. The reconstructed images were then quality checked by both Nikon Elements and by the ImageJ plugin, SIMcheck, described in (Ball et al., 2015). Drift correction between channels was performed with 100 nm Tetraspec fluorescent microspheres (Molecular Probes).

Live 3D-SIM imaging of dissociated hippocampal neurons expressing GFP-Gephyrin-FingR was performed with a ludin chamber in a stage top incubator (Tokai HIT) allowing for control of temperature (37°C), humidity (100%) and CO$_2$ levels (5%). Neurons were placed in the chamber in artificial cerebrospinal fluid (ACSF; 130mM NaCl, 5mM KCL, 10 mM HEPES, 30 mM glucose, 2 mM CaCl$_2$ and 1 mM MgCl$_2$, pH 7.4) and allowed to equilibrate for 30 minutes before imaging at T0. Perfect Focus was engaged to minimize Z drift and z stacks were programed to be acquired every hour for 7 hours. For bicuculline conditions, 10 μM bicuculline was added to the ACSF immediately following T0.

STED

STED imaging was performed on a custom-built two-color system built around an Olympus IX-71 stand described in detail in (Bowen et al., 2017; Meyer et al., 2016). Briefly, excitation and STED light are generated by a fiber-based pulsed laser system (ALP-710-745-SC, Fianium Ltd.) that provides two STED laser lines at 715nm and 745nm and a white light supercontinuum output ranging from 400nm to 2000nm. The excitation wavelengths of 570nm and 647nm are selected from the supercontinuum by using a beam splitter and two bandpass interference filters (Z570/10x and HQ647/10x, Chroma Technology). The excitation and STED pulses for the red channel (570nm/715nm) are delayed with respect to the far red channel, generating an interleaved excitation and STED pulse train that sequentially excites each channel. The STED beam path passes through a vortex phase plate (VPP-1a, RPC Photonics Inc.), which results in a torus shaped STED focus in the imaging plane. A custom dichroic combines the excitation and laser beams and a high NA objective (100X, 1.4 NA UPlanSApo Oil, Olympus Inc.) focuses all four beams onto the sample. Emission light is collected by the objective and the two-color channels are spectrally separated using a dichroic (T650lpxr, Chroma Technology) and emission filters remove any additional background (Atto 647N: HQ660LP, HQ675/50M and HQ620/40M, Atto 590: HQ680/40M-HC, Chroma Technology) before coupling into two 62.5-μm core multimode fibers (M31L01, Thorlabs Inc.). Each multi-mode fiber serves as both a confocal pinhole and couples the light to an avalanche photodiode (APD) detector (SPCM-AQRH-13-FC, Perkin Elmer, Inc.). The interleaved excitation pattern allows for time-gating the two color channels, which drastically reduces fluorescence bleed through. The image is constructed by stage scanning, using a high-resolution 3D piezoelectric stage that scans the sample with a maximum 30 μm x-y travel and 10 μm z travel (P-733.3DD, Physik Instrumente) with an analog/digital controller (E-725.3CDA, Physik Instrumente). Custom ordered 40 nm beads from Life Technologies labeled with red and far red dyes (proprietary) were used for resolution calculations and system alignment.

Confocal

Confocal images were acquired on Zeiss a 700 upright confocal microscope using a 63X, 1.4 NA oil objective and digitally captured using LSM software.

Image analysis

Image Segmentation

As many synaptic ROIs were manually selected from images as possible: all synapses had to be completely encompassed within the Z stack and include all channels imaged (i.e., GABA$_A$R, gephyrin and either VGAT or RIM). For live imaging, all possible synapses

were chosen at T0 and then discarded if they were not encompassed within the z stack at any point during the time-course. Selected synapses were from dendrites of neurons with pyramidal morphology and analyzed blind to condition.

Typically, 10-15 ROIs (synapses) per image (neuron) were generated. In order to quantitatively characterize synaptic architecture and organization in an unbiased fashion, we implemented a semi-automated computational analysis pipeline, facilitating both reproducibility and data throughput. Subsynaptic features were delineated by utilizing a model-based image segmentation methodology based on a split-Bregman algorithm first described in (Paul et al., 2013) and subsequently incorporated into the MOSAIC image processing suite for ImageJ/FIJI (http://mosaic.mpi-cbg.de/(Rizk et al., 2014)). Prior to segmentation, ROIs were background corrected utilizing a histogram-based background estimator, also implemented as part of the MOSAIC suite. Parameters for the background subtraction and segmentation were determined heuristically for each labeling protocol and sample type by evaluating the segmentation outcomes across a sub-set of synaptic ROIs from the larger datasets. Once determined, these parameters were held constant across all images and conditions being compared. Objects in the ROI located outside the synapse of interest (determined based on manual annotation of segmented features) were filtered and excluded from further analysis.

Geometric Analysis of Synaptic Features

3D Binary masks were imported into MATLAB using the [loadtiff] function (FileExchage: Multipage TIFF stack). Geometric characterization of individual objects (e.g., volume, number, x-y-z coordinates) were then determined via the [regionprops] function (Image Processing Toolbox). Distances between the geometric object centers (all possible inter-compartment pairwise combinations) were calculated using the [pdist] function. Compartment volumes, the volume encompassing all objects of a certain type (e.g., all gephyrin objects; all postsynaptic objects: gephyrin + GABA$_A$Rs), were determined by calculating the convex hull for the combined point-clouds of all objects in the compartment of interest (the [convhull] function in MATLAB). Overlap between objects was calculated as part of the Mosaic Suite segmentation methodology, however we compiled this data to exclude filtered objects.

For the RIM/GABA$_A$R pairing analysis we identified the maximum intensity point within each SSD. The binary mask created by the object-segmentation was applied to the original intensity image, creating an object-bound intensity map. The center points of regional intensity maximum were then identified using the MATLAB function [imregionalmax]. The nearest neighbor regional intensity max point pairs in the corresponding channels (RIM and GABA$_A$R) were assigned based on the [knnsearch] function in MATLAB.

To ensure realistic synaptic geometries and object numbers, randomized data for coupling analysis was generated on a ROI to ROI basis. The synaptic compartments (see Figure 2) were used to create a bounding box for the randomized points, the number of which were set to match the number of objects in the experimental data for that ROI.

QUANTIFICATION AND STATISTICAL ANALYSIS

All statistical tests were performed in Prism7 (GraphPad). Data were tested for normality with D'Agostino and Pearson to determine use of non-parametric (Mann-Whitney, Kruskal-Wallis, Spearman correlations), or parametric (unpaired t test, ANOVA, Pearson's correlations) tests. Post hoc tests were included in analyses with multiple comparisons. Bar graphs are displayed as mean ± SEM, unless otherwise noted. Box-plots are displayed as the median (horizontal line), the 25th and 75th percentiles (upper and lower bounds of the box), maximum and minimum values excluding outliers (maximum and minimum whiskers) and the cross represents the mean. P values were considered significant if < 0.05. N numbers refer to number of synapses per condition unless otherwise stated.

Supplemental Information

Nanoscale Subsynaptic Domains Underlie

the Organization of the Inhibitory Synapse

Kevin C. Crosby, Sara E. Gookin, Joshua D. Garcia, Katlin M. Hahm, Mark L. Dell'Acqua, and Katharine R. Smith
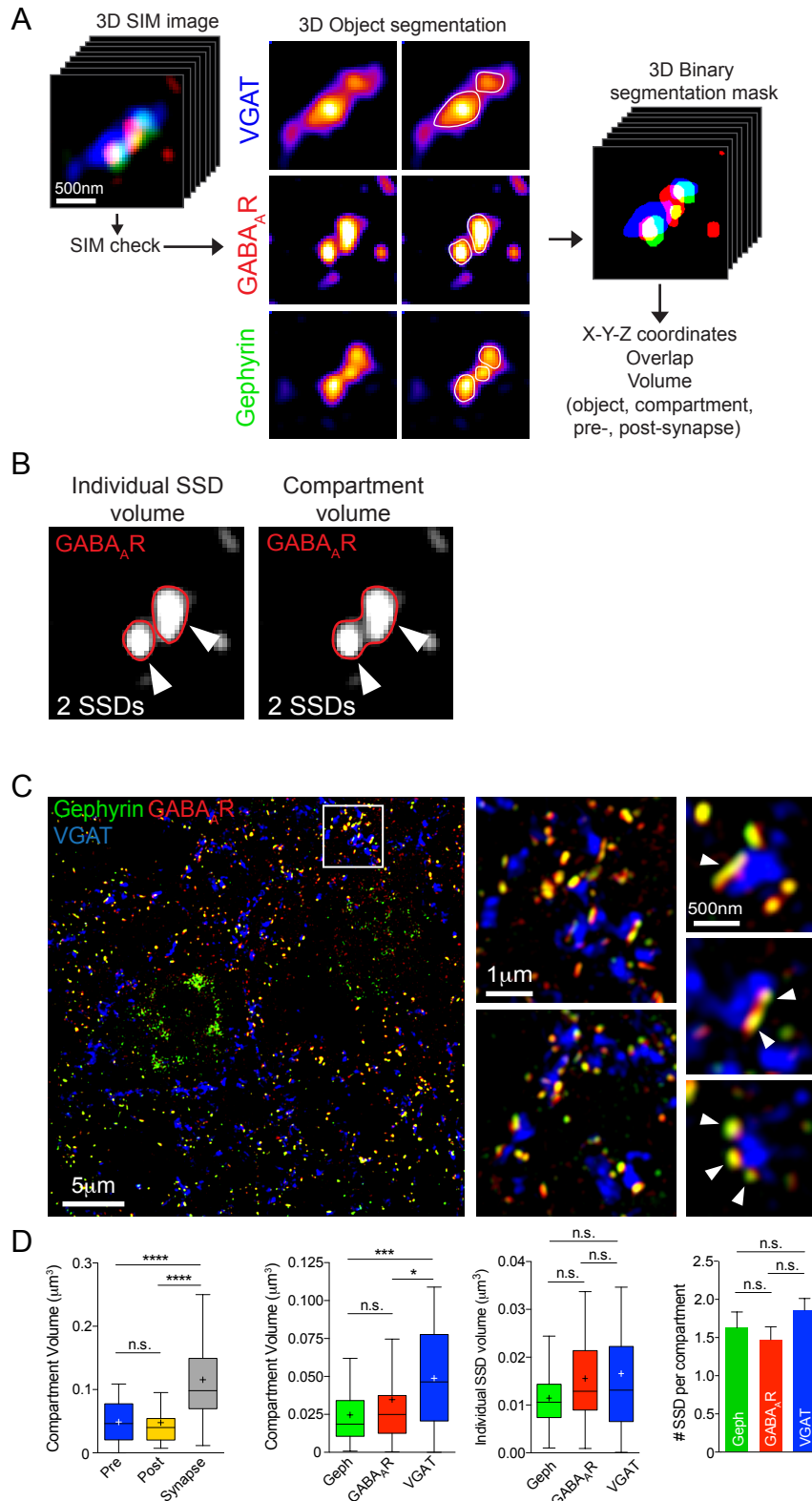
Figure S1 Related to Figure 2. 3D segmentation analysis of SIM images and 3D-SIM in acute brain slices. A. 3D segmentation protocol of 3D-SIM image, providing binary segmentation mask from which numerous parameters can be extracted. **B**. Representation of measurements of 'individual SSD volume' and 'compartment volume' for a GABA$_A$R compartment with 2 SSDs.

C. Maximum projection SIM image of cortical slice (layer 2/3) labeled with antibodies to gephyrin, GABA$_A$Rs and VGAT. White boxes highlight magnified regions. **D.** Quantification of compartment volume, individual SSD volume and number of SSDs per synapse, n=58 synapses, 10 neurons, Kruskal-Wallis tests. Cross denotes mean, horizontal line denotes median.
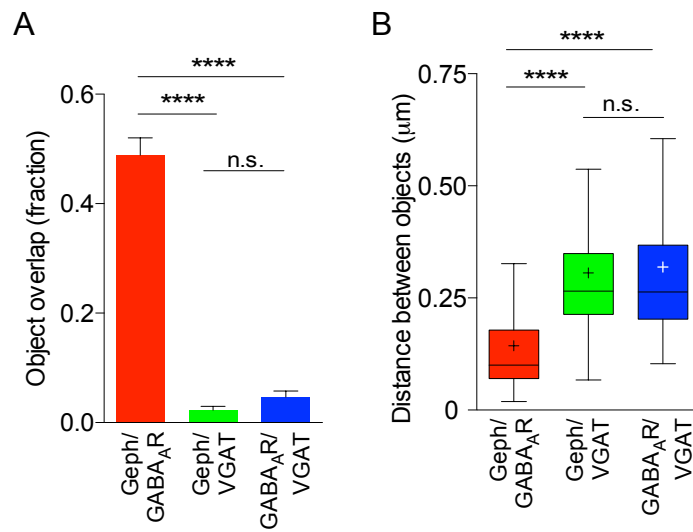
Figure S2 Related to Figure 3. Overlap and distance analysis of inhibitory synapses in acute brain slices.
A. Mean overlap fraction for gephyrin, $GABA_ARs$ and VGAT, $p^{****}<0.0001$, Kruskal-Wallis, n= 58 synapses. Data are represented as mean ± SEM.
B. Box plot of center-to-center distances between neighboring SSDs, $p^{****}<0.0001$, Kruskal-Wallis, n=83-89 SSDs. Cross denotes mean, horizontal line denotes median.

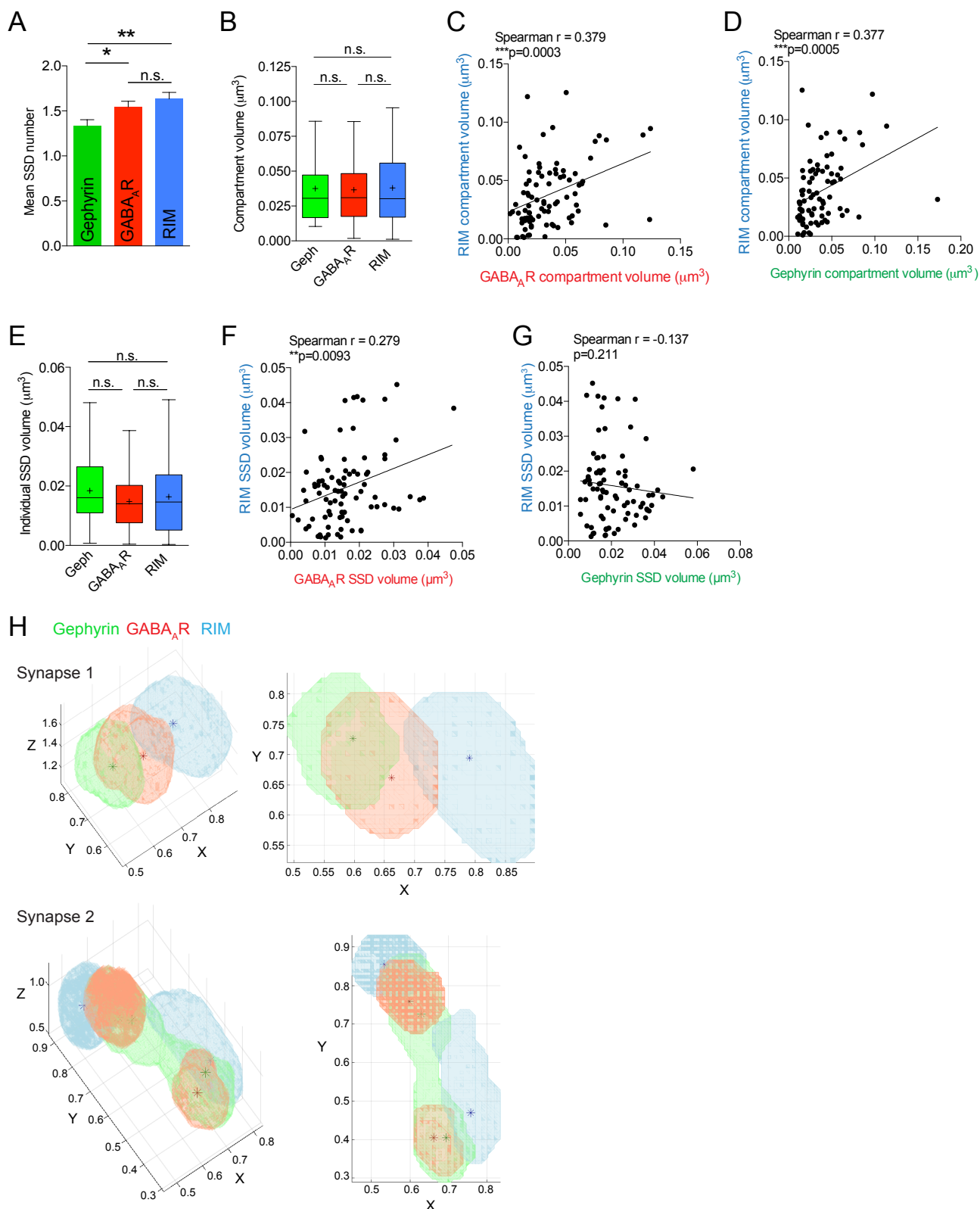**Figure S3 Related to Figure 5. Volume data for gephyrin, GABA$_A$Rs and RIM SSDs.**

A. Mean number of SSDs per compartment for gephyrin, GABA$_A$R and RIM, p***<0.0010, Kruskal-Wallis, Dunn's post hoc, n=92 synapses. Data are represented as mean ± SEM.

B. Box plot of compartment volumes for gephyrin, GABA$_A$R and RIM, n.s., Kruskal-Wallis, Dunn's post hoc, n= 92 synapses. Cross denotes mean, horizontal line denotes median.

C. Correlation plot of RIM compartment volume and GABA$_A$R compartment volume per synapse, n= 92 synapses.

D. Correlation plot of RIM compartment volume and gephyrin compartment volume per synapse, n= 92 synapses.

E. Box plot of individual SSD volumes for gephyrin, GABA$_A$R and RIM, n.s, Kruskal-Wallis, Dunn's post hoc, n= 92 synapses. Cross denotes mean, horizontal line denotes median.

F. Correlation plot of RIM individual SSD volume and GABA$_A$R individual SSD volume per synapse, n= 92 synapses.

G. Correlation plot of RIM individual SSD volume and gephyrin individual SSD volume per synapse, n= 92 synapses.

H. Further examples of 3D and 2D rendering of inhibitory synapses. Stars denote maximun intensity points, units=μm.
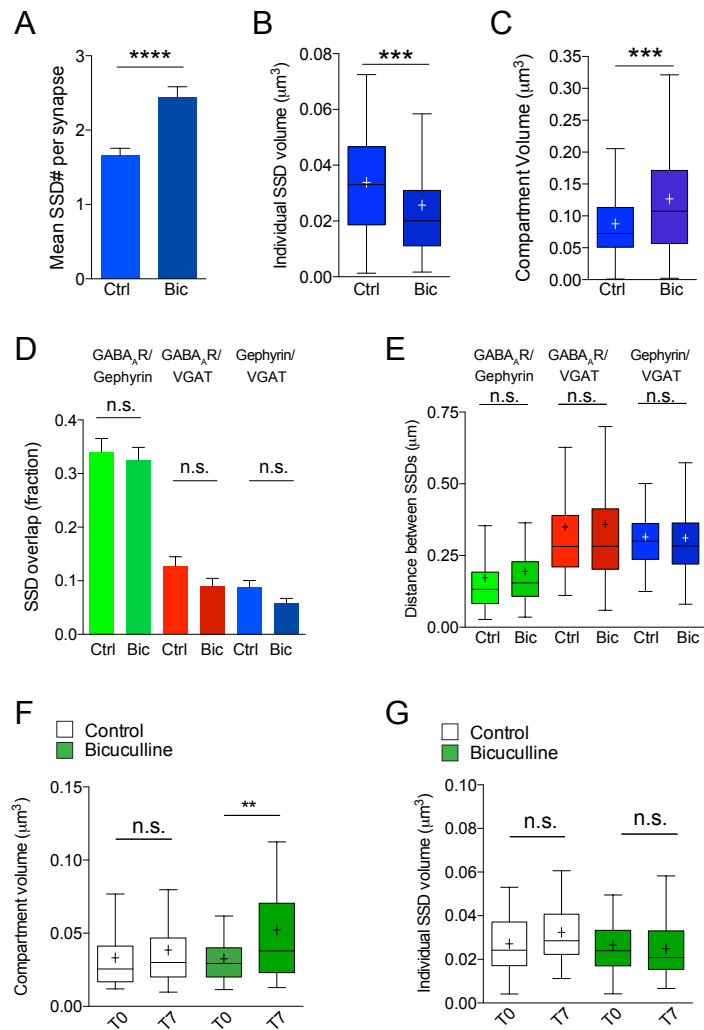
Figure S4 Related to Figure 6. Further measurements of inhibitory synapses.
A. Mean number of SSDs per VGAT compartment in control or bicuculline treated conditions.,****p<0.0001, n= 85/97 synapses, Mann-Whitney test. Data are represented as mean ± SEM.
B. Box plot of VGAT individual SSD volume in control and bicuculline conditions, ***p=0.0001,
n= 85/97 synapses, Mann-Whitney test. Cross denotes mean, horizontal line denotes median.
C. Box plot of VGAT compartment volume in control and bicuculline conditions, p=0.002, n= 48/73 synapses, t-test. Cross denotes mean, horizontal line denotes median.
D. Mean overlap fraction for gephyrin, GABA$_A$Rs and VGAT in control or bicuculline (Bic) treated conditions. Data are represented as mean ± SEM.
E. Box plot of center-to-center distances between neighboring SSDs for gephyrin, GABA$_A$Rs and VGAT in control or bicuculline treated conditions. Cross denotes mean, horizontal line denotes median.
F. Box plot of gephyrin compartment volume in control and bicuculline conditions at time 0 and 7 hours, p=0.002, n= 48/73 synapses, t-test. Cross denotes mean, horizontal line denotes median.
G. Box plot of gephyrin individual SSD volume in control and bicuculline conditions at time 0 and 7 hours, p>0.05, n= 48/73 synapses, t-test. Cross denotes mean, horizontal line denotes median.